Neurogenesis in the Striatum of the Adult Human Brain.

Aurélie Ernst, Kanar Alkass, Samuel Bernard, Mehran Salehpour, Shira Perl, John Tisdale, Göran Possnert, Henrik Druid, Jonas Frisén

Cell

Neurogenesis in the Striatum of the Adult Human Brain

Aurélie Ernst,[1] Kanar Alkass,[1,2] Samuel Bernard,[3] Mehran Salehpour,[4] Shira Perl,[5] John Tisdale,[5] Göran Possnert,[4] Henrik Druid,[2] and Jonas Frisén[1,*]
[1]Department of Cell and Molecular Biology
[2]Department of Oncology-Pathology
Karolinska Institute, 171 77 Stockholm, Sweden
[3]Institut Camille Jordan, CNRS UMR 5208, University of Lyon, 69622 Villeurbanne, France
[4]Department of Physics and Astronomy, Ion Physics, Uppsala University, 751 20 Uppsala, Sweden
[5]NHLBI, NIH, Bethesda, Maryland 20892, USA
*Correspondence: jonas.frisen@ki.se
http://dx.doi.org/10.1016/j.cell.2014.01.044

SUMMARY

In most mammals, neurons are added throughout life in the hippocampus and olfactory bulb. One area where neuroblasts that give rise to adult-born neurons are generated is the lateral ventricle wall of the brain. We show, using histological and carbon-14 dating approaches, that in adult humans new neurons integrate in the striatum, which is adjacent to this neurogenic niche. The neuronal turnover in the striatum appears restricted to interneurons, and postnatally generated striatal neurons are preferentially depleted in patients with Huntington's disease. Our findings demonstrate a unique pattern of neurogenesis in the adult human brain.

INTRODUCTION

The generation of new neurons in the adult brain serves to maintain a pool of neurons with unique properties, present for a limited time after their birth, which enable specific types of neural processing (Ge et al., 2007; Schmidt-Hieber et al., 2004). Adult neurogenesis is important for pattern separation in memory formation and odor discrimination in rodents (Clelland et al., 2009; Nakashiba et al., 2012; Sahay et al., 2011), and alterations in adult neurogenesis are implicated in psychiatric disease in humans (Eisch and Petrik, 2012; Kheirbek et al., 2012).

Whether adult neurogenesis has decreased with evolution has long been a topic of debate (Kempermann, 2012; Rakic, 1985). Humans appear unique among mammals in that there is no detectable adult olfactory bulb neurogenesis (Bergmann et al., 2012; Sanai et al., 2011). However, there is substantial hippocampal neurogenesis, with comparable neuronal turnover rates in middle-aged humans and mice (Eriksson et al., 1998; Spalding et al., 2013). A larger fraction of hippocampal neurons are subject to exchange in humans than in mice, and adult hippocampal neurogenesis shows a much less dramatic decline with aging in humans compared to mice (Spalding et al., 2013).

It may appear intuitive that hippocampal neurogenesis has been retained during human evolution, to provide cognitive adaptability, and that olfactory bulb neurogenesis has decreased with the reduced dependence on olfaction in humans compared to our predecessors. However, neuronal precursor cells (neuroblasts) are generated not only in the hippocampus but also in the lateral ventricle wall in adult humans, the site of origin of olfactory bulb neurons in other mammals. The extent and dynamics of neuroblast generation in humans in these two regions are remarkably similar, with a dramatic decline during the first postnatal months, followed by sustained generation, decreasing slowly with age (Göritz and Frisén, 2012; Knoth et al., 2010; Sanai et al., 2011). The difference between humans and other mammals is thus not the pattern of neuroblast generation but that the neuroblasts generated in the lateral ventricle wall neurogenic niche do not migrate to the olfactory bulb. The fate of neuroblasts born in the human lateral ventricle wall has been unknown.

We here report that neuroblasts are not restricted to the lateral ventricle wall in humans but that they are also present in the adjacent striatum. Retrospective birth dating revealed continuous generation of striatal interneurons in humans. In Huntington's disease, a neurodegenerative disease affecting striatal neurons (Walker, 2007; Zuccato et al., 2010), we find that postnatally generated neurons are absent in advanced stages of the disease. This identifies a unique pattern of adult neurogenesis in humans.

RESULTS

Neuroblasts in the Adult Human Striatum

The finding that neurons are not added in the olfactory bulb of adult humans (Bergmann et al., 2012), in spite of the generation of neuronal precursors in the subventricular zone (Sanai et al., 2011; Wang et al., 2011), posed the question of whether neuroblasts may migrate to another location close to the ventricle. Analysis of transcriptome data available from a large number of developing and adult human brains (Kang et al., 2011) demonstrated that the expression of *doublecortin (DCX)*, a commonly used neuroblast marker, was at least as high in the adult human

striatum as in the hippocampus (Figure 1A and Table S1 available online). Only background levels were detected in the nonneurogenic adult cerebellum (Figure 1A, Table S1). When comparing *DCX* expression levels in the striatum with other brain regions close to the lateral ventricle, high *DCX* mRNA levels were specific to the striatum in the data from Kang et al. (2011) as well as in an additional human transcriptome data set (Figure S1F). *DCX* transcript levels in the human hippocampus correlate closely with the number of neuroblasts at different ages (Kang et al., 2011) and the number of DCX-positive cells in the hippocampus in turn correlates with the number of newly generated neurons (Spalding et al., 2013).

Western blot analysis of the human postmortem hippocampus, striatum, and cerebellum from subjects aged 21 to 68 years showed that DCX and polysialylated neural cell adhesion molecule (PSA-NCAM), another marker associated with neuroblasts, were as abundant in the striatum as in the hippocampus, and low to undetectable in the adult cerebellum (Figure 1B). This is in line with a previous study demonstrating DCX and PSA-NCAM by western blot in the adult human striatum, with similar levels in the caudate nucleus and putamen (Tong et al., 2011).

Immunohistochemistry revealed DCX-positive putative neuroblasts in the adult human dentate gyrus of the hippocampus and in the subventricular zone of the lateral wall of the lateral ventricle (Figure S1), in line with previous studies (Knoth et al., 2010; Sanai et al., 2011; Wang et al., 2011). DCX-positive cells were also present in the caudate nucleus and the putamen of striatum (Figures 1C–1F). The morphology of the DCX-positive cells in the striatum varied from rounded without processes, elongated with few processes to highly branched (Figures 1C–1F), similar to the neuroblasts in the subventricular zone and hippocampus (Knoth et al., 2010; Sanai et al., 2011; Wang et al., 2011). The DCX-positive cells in the striatum were most often found as single isolated cells, and there were no apparent streams of potentially migratory cells from the subventricular zone. Most of the DCX-positive cells in the dentate gyrus, subventricular zone, and striatum were also positive for PSA-NCAM and the neuronal marker NeuN, but they were invariably negative for the astrocytic marker GFAP (Figure 1C and S1, Table S2). The presence of the mature neuronal marker NeuN in many DCX-positive neurons does not necessarily imply that they are not newborn; in nonhuman primates, adult-born neurons in the dentate gyrus maintain DCX for at least 6 months and coexpress NeuN (Kohler et al., 2011), suggesting that they may retain a juvenile state for a substantial period of time.

The five main neuronal subtypes in the striatum can be identified by the markers dopamine- and cAMP-regulated neuronal phosphoprotein (DARPP32), calretinin, choline acetyltransferase, parvalbumin, and neuropeptide Y. DCX most commonly colocalized with calretinin and more rarely with neuropeptide Y (Figures 1D and 1E, Table S2), whereas we did not find any colocalization with markers for the other subtypes. We did not detect DCX-positive cells with the apoptotic marker activated caspase-3 in the subventricular zone or striatum. In contrast, cleaved caspase-3 was detected in some DCX-positive cells in the subventricular zone of subjects with Huntington's disease (Figures S1B–S1E).

New Neurons in the Adult Human Striatum

Over time, cells accumulate the age pigment lipofuscin, consisting of autofluorescent matrix and lipid droplets (Sulzer et al., 2008). There are no definitive molecular markers for neuroblasts, and some nonrenewing neurons have been reported to express DCX (Klempin et al., 2011; Plümpe et al., 2006) or PSA-NCAM (Nacher et al., 2002; Seki, 2002). However, most DCX-positive cells in the striatum were devoid of lipofuscin (Figure 1F), suggesting that they are indeed newly generated cells, and those that did have lipofuscin contained only a few granules. The vast majority of the hippocampal neurons of the granular zone of the dentate gyrus also lack lipofuscin in adult humans (Table S3).

We examined lipofuscin accumulation in the five major neuronal subtypes of the human striatum. We found that 4.7% of the calretinin-expressing interneurons were devoid of lipofuscin and a larger fraction (16.8%) had low lipofuscin content in adult humans (Figures 2A and 2B). A similar fraction of NPY-positive neurons had a low lipofuscin content (19.5%), but only very few (0.6%) were completely devoid of lipofuscin. The other neuronal subclasses were dominated by cells with high lipofuscin content, and we failed to find any such cells devoid of lipofuscin. It is not possible to deduce the age of a cell based on its lipofuscin content. However, we did not find any lipofuscin in striatal neurons in a 9-month-old subject, whereas >96% of striatal neurons contained lipofuscin in a 2.8- and a 6-year-old individual (as well as in all older studied subjects), suggesting that it may take a few years for newborn striatal neurons to accumulate lipofuscin (Table S3).

Thymidine analogs incorporated into the DNA of dividing cells can be detected in their progeny, allowing for the identification of newly generated cells. We analyzed postmortem tissue from the striatum, hippocampus, and cortex from cancer patients who received iododeoxyuridine (IdU) for radiosensitization (see Table S4 for information on the patients). In patients receiving the lowest IdU concentrations, we failed to detect any IdU-labeled cells, neuronal or nonneuronal, in the brain. However, in all individuals in whom we found IdU-labeled nonneuronal cells (n = 4 subjects, age 20–71), we also detected IdU-labeled cells in the striatum coexpressing the neuronal markers NeuN, MAP2, and/or calretinin (Figures 2C–2E). IdU-labeled neurons were found in both the caudate nucleus and the putamen. The nuclei of IdU-positive cells were uniformly labeled, and not in a punctuate pattern, the later being associated with DNA repair. IdU-positive neurons were also detected in the dentate gyrus of the hippocampus in the same subjects (Figure S2), but not in the cerebral cortex, in line with previous studies (Bhardwaj et al., 2006; Eriksson et al., 1998).

Retrospective Birth Dating of Striatal Cells

It is difficult to estimate the dynamics of neurogenesis based on the incorporation of labeled nucleotides. This is especially true in humans, as the access to tissue is very limited and it is inevitable that the subjects receive different doses at different times prior to their death. In order to explore turnover dynamics of cells in humans, we have developed a method to retrospectively birth date cells, which is based on the integration of

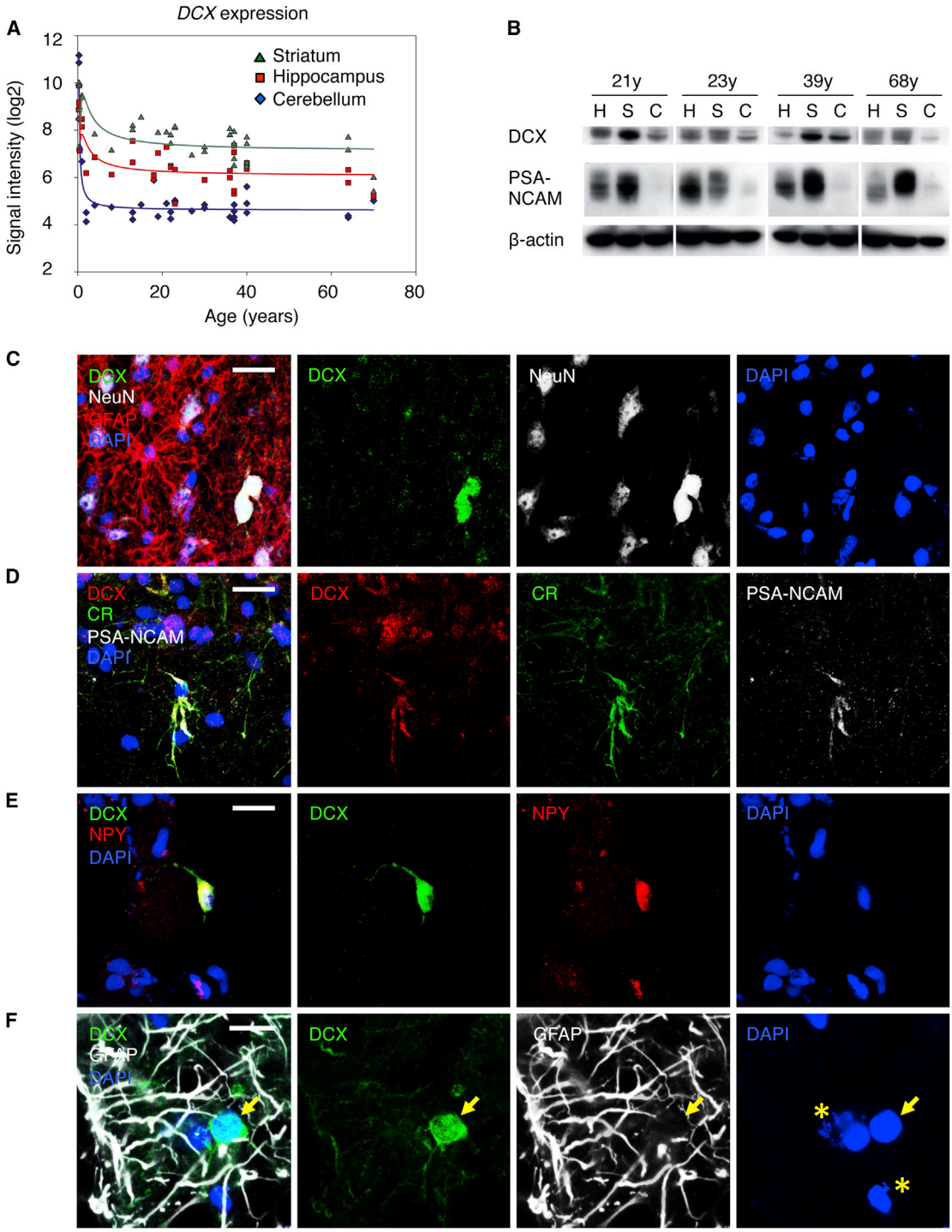

Figure 1. Neuroblasts in the Adult Human Striatum

(A) *DCX* expression in the striatum (green), hippocampus (red), and cerebellum (blue) across the human lifespan. Data from Kang et al. (2011). The striatal area used for the transcriptome analysis comprises the caudate nucleus (lateral ventricle wall included), the nucleus accumbens, and the putamen. See also Table S1.

(B) Western blot analysis of DCX, PSA-NCAM and β-actin in the hippocampus (H), striatum (S), and cerebellum (C) of human subjects of different ages.

(C–F) Confocal microscopy of DCX-positive cells in the striatum. The majority of the DCX-positive cells express the mature neuronal marker NeuN but all of them lack expression of the astrocytic marker GFAP (C). Most of the DCX-positive cells also express PSA-NCAM (D). DCX occasionally colocalizes with neuronal

(legend continued on next page)

nuclear-bomb-test-derived ^{14}C in DNA of proliferating cells (Figure 3A) (Spalding et al., 2005).

We isolated cell nuclei from the human postmortem lateral wall of the lateral ventricle and from the striatum by gradient centrifugation. Analysis of the ^{14}C concentration in their genomic DNA by accelerator mass spectrometry revealed levels corresponding to time points after the birth of the individuals, showing that there is postnatal cell turnover in the human striatum and in the lateral wall of the lateral ventricle (Figure 3B and Table S5). There was no significant difference in cell turnover in the striatum and in the lateral ventricle wall ($p = 0.71$, two-tailed Mann-Whitney test). In line with a population comprising several cell types, subpopulation dynamics analysis pointed to a heterogeneous group of cells, with some subpopulations having high turnover rates, others low ones, and a large proportion of cells not being exchanged at all postnatally (Figure 3C).

Adult Striatal Neurogenesis in Humans

To specifically birth date different cell types in the lateral ventricle wall and striatum, nuclei were incubated with antibodies against the neuron-specific nuclear epitope NeuN and the oligodendrocyte lineage marker SOX10. Neuronal, oligodendrocyte lineage and nonneuronal/nonoligodendrocyte lineage nuclei were isolated by flow cytometry (Figures 4 and S3) (Bergmann et al., 2012; Spalding et al., 2013). Reanalysis by flow cytometry and analysis of mRNA expression indicated the specificity of the isolation (Figure S3). The ^{14}C concentration in genomic DNA from neurons ($n = 30$ individuals), oligodendrocyte lineage cells ($n = 28$), and nonneuronal/nonoligodendrocyte lineage cells ($n = 26$) was measured in subjects from 3 to 79 years of age (^{14}C data are given in Table S5).

First, we analyzed the ^{14}C concentration in neuronal genomic DNA in the lateral wall of the lateral ventricle and in the striatum (Figure 4C). For the majority of the analyzed subjects, the ^{14}C concentration in neuronal genomic DNA corresponded to the concentration in the atmosphere after the birth of the individual, showing the postnatal generation of striatal neurons. In contrast, cortical, cerebellar and olfactory bulb neurons are not renewed postnatally to a detectable level in humans, and ^{14}C levels in their DNA correspond to the time around the birth of the individual (Figure S3) (Bergmann et al., 2012; Bhardwaj et al., 2006; Spalding et al., 2005). Individuals born before the nuclear bomb tests had lower ^{14}C levels in striatal neuron DNA than at any time after 1955, establishing that although some neurons are generated postnatally, a large majority of striatal neurons are not exchanged after birth. Mathematical modeling of ^{14}C data allows a comprehensive analysis of cell turnover (Bergmann et al., 2009; Bergmann et al., 2012; Spalding et al., 2013). By fitting several mathematical models to the data, the cell renewal rate and the fraction of cells showing turnover were estimated (see Table S6 and Extended Experimental Procedures). The best model was a scenario in which a subpopulation of the neurons is renewing, whereas the majority is not. The size of the cycling neuronal population was 25% (95% confidence interval: 6%–51%). Individual estimates of turnover rates showed a modest decline in turnover over age within the cycling population (Figure 4D). The median turnover rate of neurons within the renewing fraction was 2.7% per year in adulthood, which is not significantly different ($p = 0.7$, two-tailed Mann-Whitney test) compared to the turnover rate of neurons within the renewing fraction in the adult human hippocampus (Spalding et al., 2013).

Turnover of Striatal Interneurons

Given that a large proportion of striatal neurons are not renewed postnatally, we next wanted to identify the subset of striatal neurons that is subject to exchange. The medium spiny projection neurons make up 75%–80% of the striatal neurons, and the four subtypes of interneurons together represent 20%–25% of the striatal neurons (Cicchetti et al., 2000). However, it is not feasible to separately carbon date each of these five neuronal populations with the current sensitivity of accelerator mass spectrometry. For this reason, we aimed at independently carbon dating medium spiny neurons and interneurons. It is challenging to isolate these populations at high purity and therefore not possible to obtain robust quantitative estimates; however, it can point to which neuronal fraction the turnover is in. Striatal nuclei were incubated with antibodies against the neuron-specific nuclear epitope NeuN and the medium spiny neuron marker DARPP32. Nuclei of medium spiny neurons (NeuN+/DARPP32+), interneurons (NeuN+/DARPP32−) and nonneuronal cells (NeuN-) were isolated by flow cytometry (Figure 5 and Figure S4). The ^{14}C concentration in genomic DNA from medium spiny neurons ($n = 26$ individuals), interneurons ($n = 11$), and nonneuronal cells ($n = 18$) was measured by accelerator mass spectrometry (^{14}C data are given in Table S5).

^{14}C levels in medium spiny neuron DNA corresponded to the time around the birth for most of the individuals (Figure 5C), showing that this subtype of striatal neurons is probably not renewed postnatally to a significant level. This finding is in line with the presence of the age pigment lipofuscin in all medium spiny neurons as well as the lack of colocalization of DARPP32 with neuroblast markers or IdU (Figures 1 and 2). In contrast, the ^{14}C concentration in genomic DNA from interneurons corresponded to time points after the birth of the individuals for the majority of the analyzed subjects (Figure 5D), demonstrating postnatal generation of striatal interneurons. Modeling indicates that the striatal neuronal turnover occurs within the interneuron fraction (Table S6).

Turnover of Nonneuronal Cells

Next, we assessed the turnover dynamics of nonneuronal cells (NeuN-), oligodendrocyte lineage cells (SOX10+), and nonneuronal/nonoligodendrocyte lineage cells (NeuN-/SOX10-) in the lateral wall of the lateral ventricle and in the striatum (Figures 6 and S5). The ^{14}C concentration in genomic DNA of all of these

markers calretinin (CR) (D) and NPY (E). Most DCX-positive cells have little or no lipofuscin (arrow), whereas the majority of DCX-negative cells contain lipofuscin pigments (stars) (F). Autofluorescent lipofuscin pigments are not visible in all channels because an antiautofluorescence treatment was applied. Scale bars, 20 μm for (C)–(E) and 10 μm for (F). Cell nuclei are labeled with DAPI and appear blue.
See also Figure S1 and Table S2.

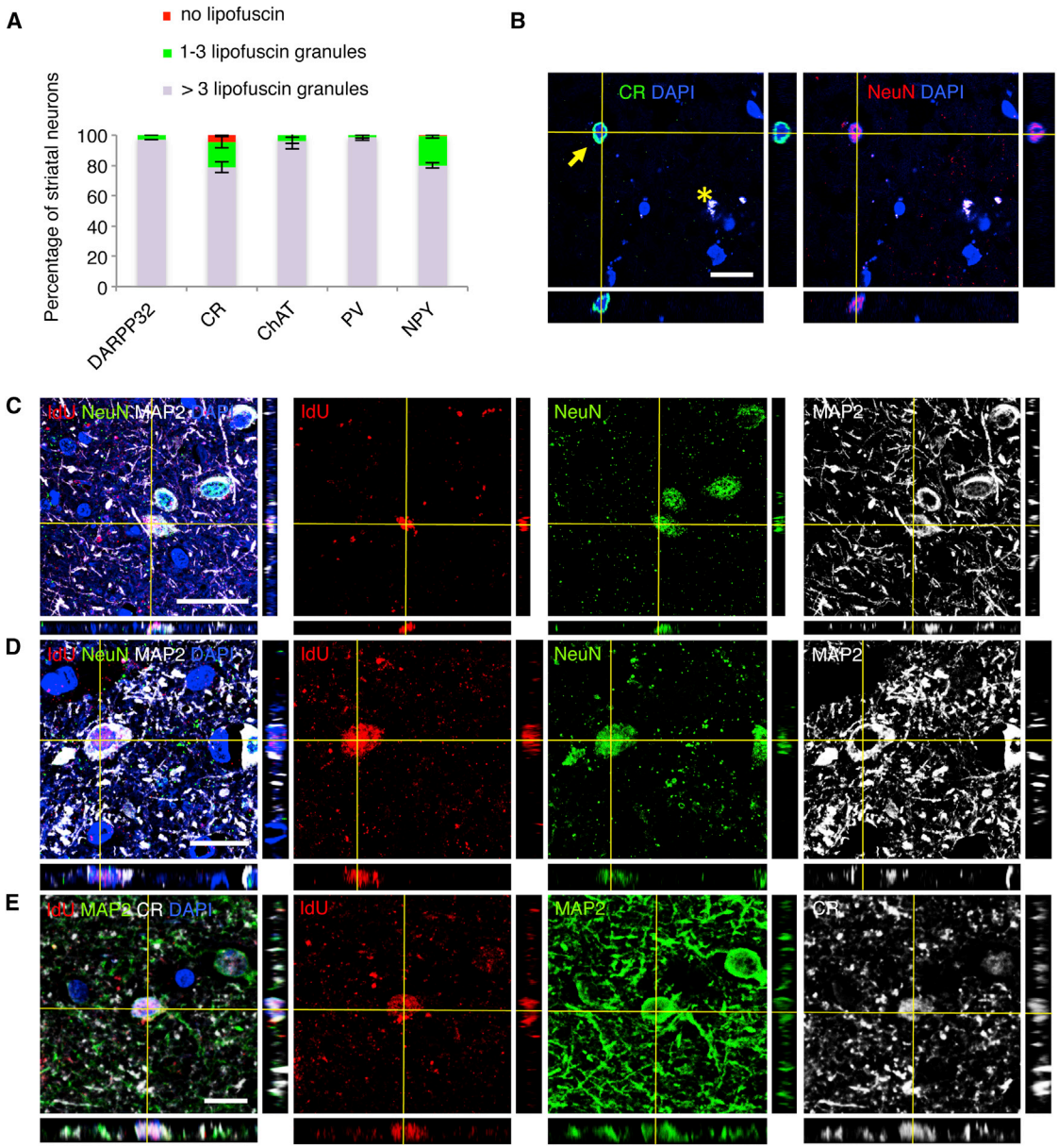

Figure 2. New Neurons in the Adult Human Striatum

(A) Lipofuscin quantification by confocal microscopy in the five main subtypes of striatal neurons. DARPP32, dopamine- and cAMP-regulated neuronal phosphoprotein; CR, calretinin; ChAT, Choline acetyltransferase; PV, parvalbumin; NPY, neuropeptide Y. Data are shown as mean values for three donors aged between 21 and 26. Error bars represent standard deviation. A minimum of 200 neurons per subtype and per subject were analyzed.

(B) Confocal images with orthogonal views demonstrate the absence of lipofuscin granules in a calretinin-positive neuron (arrow) while other cells have autofluorescent lipofuscin pigments in their cytoplasm, visible in all channels (star).

(C–E) Newly generated cells can be detected in the adult human striatum in patients previously receiving the thymidine analog IdU. Confocal images with orthogonal projections showing IdU-labeled neuronal nuclei in the striatum of two subjects aged 20 and 41. Neurons are identified by the expression of NeuN, MAP2 and/or calretinin (CR).

Scale bars, 20 μm. See also Figure S2 and Tables S3 and S4.

cell populations corresponded to time points after the birth of the individuals (Figures 6A–6C), establishing turnover of nonneuronal cells.

The most accurate model for oligodendrocyte lineage cells was a scenario with a high initial turnover rate and lower replacement rate of older cells, suggesting the existence of a subset of short-lived cells (Table S6). This fraction of short-lived cells may correspond to immature oligodendrocyte progenitor cells, since approximately 23% of the SOX10+ nuclei were positive for the mature oligodendrocyte marker APC, indicating that the majority

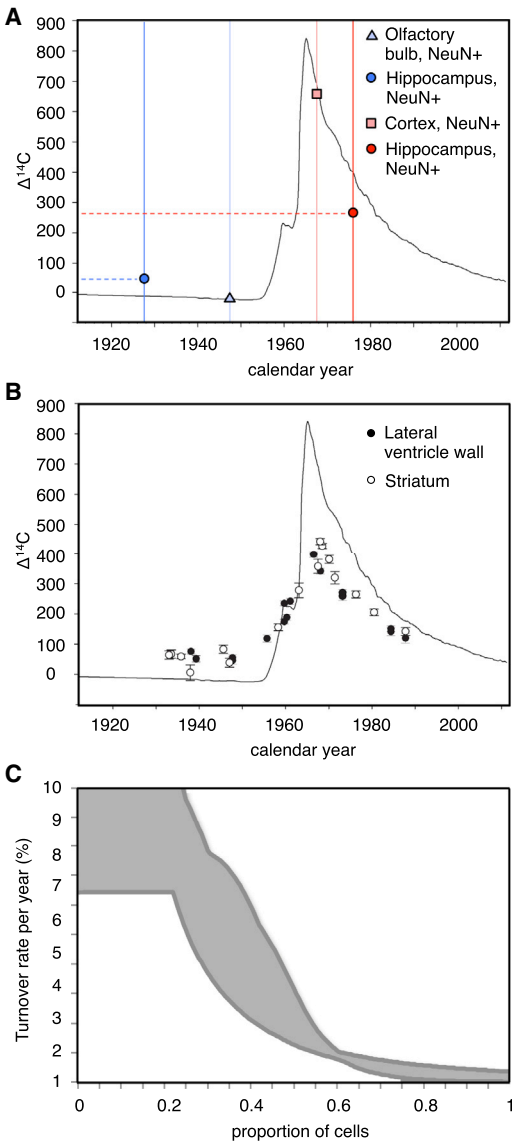

Figure 3. Postnatal Cell Turnover in the Human Lateral Ventricle Wall and in the Striatum

(A) Schematic illustration of ^{14}C concentration measurements in genomic DNA. The black line shows the atmospheric ^{14}C concentration over time. Individually measured ^{14}C concentrations in human genomic DNA are plotted at the time of the subject's birth (vertical lines), before (blue symbols) or after the ^{14}C bomb spike (red symbols). Data points above the bomb curve for subjects born before the bomb peak and below the bomb curve for subjects born after the nuclear tests indicate cell turnover. Data points on the atmospheric curve show the absence of turnover. Data from Bhardwaj et al. (2006), Bergmann et al. (2012), and Spalding et al. (2013).

(B) The ^{14}C concentrations in genomic DNA from cell nuclei isolated from the lateral wall of the lateral ventricle (black dots) and from the striatum (white dots) demonstrate postnatal cell turnover in subjects born before and after the bomb spike. Error bars indicate two standard deviations in ^{14}C concentration in the respective DNA sample.

(C) In line with a tissue composed of many different cell types, subpopulation dynamics analysis indicates that striatal cells form a heterogeneous group, some fractions having high turnover rates and some having very low ones. The gray area represents the range of acceptable values. The resolution of this type of analysis does not allow differentiating between turnover rates above 10%.

of the isolated oligodendrocyte lineage cells were progenitors. For the nonneuronal/nonoligodendrocyte lineage cells (NeuN-/SOX10−), as for the subset containing all nonneuronal cells (NeuN-), models that allowed one compartment turning over constantly and one nonrenewing population, fitted the data best (Table S6). Individual turnover estimates suggested a decline in striatal nonneuronal cell turnover during aging (Figures 6 D–6F).

Adult-Generated Neurons Are Depleted in Huntington's Disease

Huntington's disease is a neurodegenerative disorder that primarily affects the striatum. However, impaired adult hippocampal neurogenesis has been shown in patients and in transgenic rodent models of Huntington's disease (Ransome et al., 2012) and reduced adult olfactory bulb neurogenesis has been detected in a transgenic line of Huntington's disease mice (Kohl et al., 2010), despite the maintenance of the precursor and stem cell pools (Walker et al., 2011). Another study reported increased cell proliferation in the subventricular zone of Huntington's disease patients (Curtis et al., 2003). Therefore, we wanted to determine whether cell turnover dynamics might be affected in the striatum of Huntington's disease patients. Neuronal, oligodendrocyte lineage and nonneuronal/nonoligodendrocyte lineage cell nuclei were isolated from the postmortem striatum of Huntington's disease patients by flow cytometry. The ^{14}C concentration in genomic DNA from neurons (n = 11 individuals), oligodendrocyte lineage (n = 9), and nonneuronal/nonoligodendrocyte lineage cells (n = 8) was measured (^{14}C data are given in Table S5). The ^{14}C concentration in genomic DNA of oligodendrocyte lineage cells corresponded to time points after the birth of the individuals (Figure 7A), but oligodendrocyte lineage cells had significantly lower turnover rates compared to those of healthy age-matched subjects (Figure 7B).

Interestingly, the ^{14}C levels in genomic DNA of neurons from grade 2 and 3 Huntington's disease patients corresponded to the time before the onset of the nuclear bomb tests in 1955 (white dots in Figure 7C), indicating an absence of postnatally generated neurons. Two subjects with grade 1 Huntington's disease (gray dots in Figure 7C), showed slightly elevated ^{14}C levels relative to their time of birth. Striatal neurons of patients with Huntington's disease had significantly lower turnover rates compared to nonaffected age-matched subjects born in the same time frame (Figure 7D and Table S5). In line with this, we found only 1 out of 786 analyzed striatal neurons devoid of lipofuscin in subjects with Huntington's disease (Table S7). Individual turnover rates from nonneuronal/nonoligodendrocyte lineage cells were not significantly different between Huntington's disease patients and nonaffected subjects (Figures 7E and 7F), showing that the depletion of adult-born cells was specific to neurons and oligodendrocyte lineage cells in Huntington's disease.

DISCUSSION

New neurons are continuously added in the olfactory bulb and hippocampus in most mammals. Humans show substantial hippocampal neurogenesis (Spalding et al., 2013), but are unique in

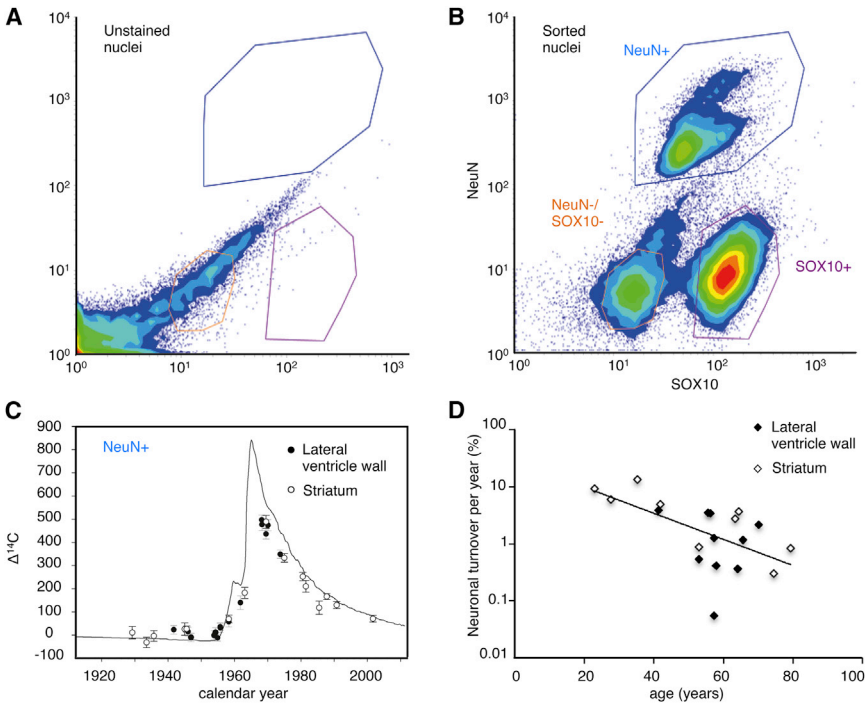

Figure 4. Neuronal Turnover Dynamics in the Lateral Ventricle Wall and in the Striatum

(A and B) Isolation of nuclei from neurons, oligodendrocyte lineage and nonneuronal/non-oligodendrocyte lineage cells from the lateral ventricle wall and from the striatum. Cell nuclei were isolated from human postmortem tissue and left unstained (A) or incubated with antibodies against the neuron-specific epitope (NeuN) and the oligodendrocyte lineage marker SOX10 (B). The neuronal (NeuN+), oligodendrocyte lineage (SOX10+) and nonneuronal/nonoligodendrocyte lineage populations (NeuN-/SOX10−) were isolated by flow cytometry. The sorting gates are indicated.

(C) ^{14}C concentrations in the lateral ventricle wall and striatal neuron genomic DNA correspond to a time after the date of birth of the individual for the majority of the analyzed subjects, demonstrating neurogenesis throughout life. Error bars indicate two standard deviations in ^{14}C concentration in the respective DNA sample.

(D) Individual turnover rates for neuronal cells computed on the basis of individual data fitting according to the 2POP scenario (see Extended Experimental Procedures). Individual turnover rates are sensitive to deviations in measured ^{14}C, especially for young individuals due to the shallow slope of the ^{14}C curve, and values <0.001 (n = 3) or >1.00 (n = 8) were excluded from the plot, but the full data are given in Table S5. The individual turnover rates for adult subjects were not significantly different between neurons from the lateral ventricle wall and from the striatum ($p = 0.9$, Mann-Whitney test) but significantly higher than the turnover rates observed in the cortex or cerebellum ($p < 0.05$, Mann-Whitney test). See also Figure S3 and Table S6.

that there is no detectable addition of neurons in the olfactory bulb. However, the density of neuroblasts is very similar in the subventricular zone and the dentate gyrus of the hippocampus. We report that cells expressing the neuroblast markers DCX and PSA-NCAM are present not only in the adult human subventricular zone, but also in the adjacent striatum. IdU in striatal interneurons indicate the generation of this cell type in adult humans and retrospective birth dating of striatal neurons confirms the generation of interneurons. We furthermore report that adult-generated striatal neurons are preferentially depleted in Huntington's disease. The identification of continuous generation of striatal interneurons identifies a unique pattern of adult neurogenesis in humans.

It is important to consider alternative interpretations of our results. Both the integration of IdU and ^{14}C monitor DNA synthesis during cell proliferation. However, chromosomal damage and repair can result in DNA synthesis. Since DNA damage and repair occur almost exclusively during the cell cycle, this would not affect the outcome of our analysis. DNA repair is thought to be very limited in postmitotic cells, and well below the detection limit of carbon dating (Spalding et al., 2005). We have not been able to detect any incorporation of ^{14}C in DNA over several decades in cerebellar, cortical, or olfactory bulb neurons in humans (Bergmann et al., 2012; Bhardwaj et al., 2006). Even ^{14}C concentrations in genomic DNA from cortical neurons after ischemic stroke, which induces massive DNA damage, are not significantly different from that present in the atmosphere at the time of birth of the individuals (unpublished data). Mathematical modeling established that the integration of ^{14}C in DNA is limited to a subpopulation of neurons, and if the DNA synthesis would be due to DNA damage and repair, these neurons would have to have exchanged their entire genomes, which appears highly unlikely. The finding that neurons in a distinct striatal subpopulation express neuroblast markers, lack age pigment, and are labeled with IdU and ^{14}C, together lend strong support to the conclusion that striatal neurons are generated in adulthood in humans.

The vast majority of neurons generated in the subventricular zone in rodents integrate in the olfactory bulb. There are, however, reports suggesting the generation of small numbers of striatal neurons in nonhuman primates (Bédard et al., 2002a; 2002b; Tonchev et al., 2005) and of calretinin-positive striatal interneurons in rats and rabbits (Dayer et al., 2005; Luzzati et al., 2006). It is well documented that substantial numbers of striatal neurons are generated from the subventricular zone in both rodents and monkeys in response to stroke (Arvidsson et al., 2002; Hou et al., 2008; Tonchev et al., 2005; Tonchev et al., 2003; Wei et al., 2011). Thus, although the olfactory bulb is the principal destination of subventricular zone neuroblasts in most mammals, there may be limited striatal neurogenesis under homeostatic conditions and more abundant in response to stroke. It appears likely that the neuroblasts and new neurons in the adult human striatum derive from the subventricular zone, although we cannot exclude other origins. One major difference between rodents and humans may thus be the direction of neuroblast migration from the subventricular zone. Altered expression of a single-axon guidance molecule is

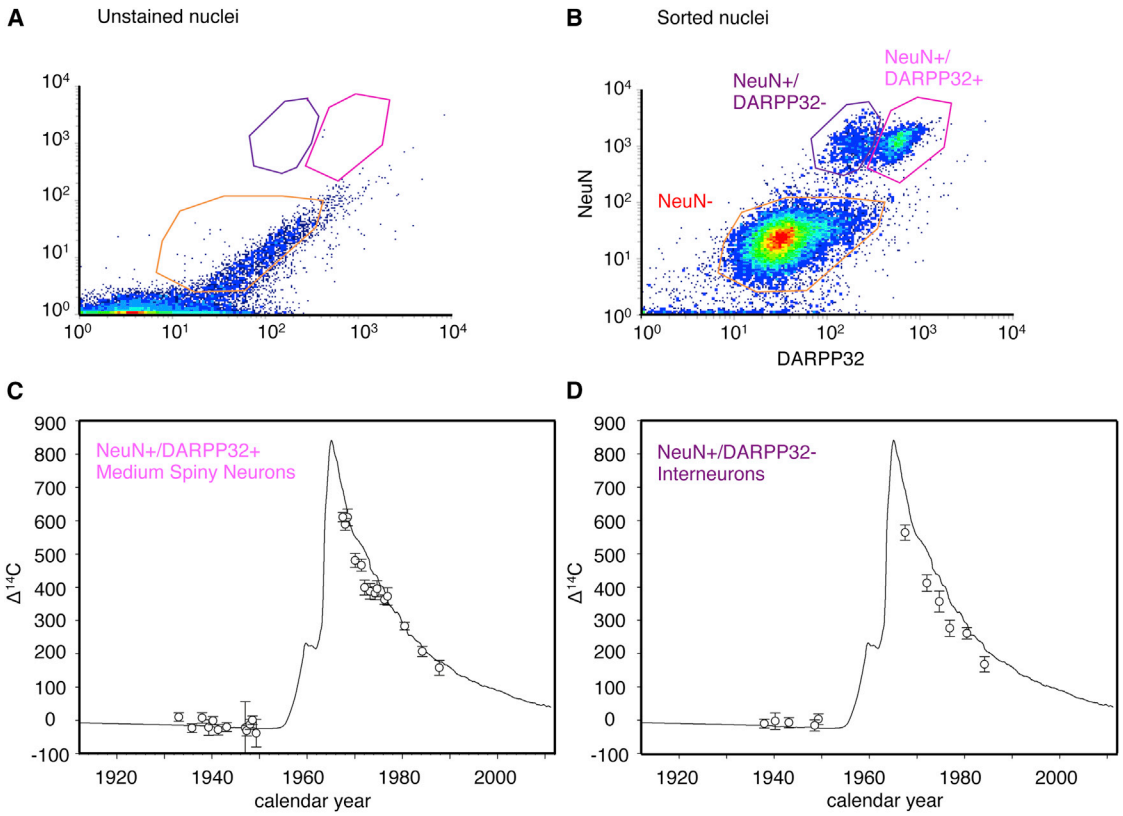

Figure 5. Turnover of Striatal Interneurons

(A and B) Cell nuclei were isolated from the human postmortem striatum and left unstained (A) or incubated with antibodies against NeuN and against the medium spiny neuron marker DARPP32 (B). The interneuron (NeuN+/DARPP32−), medium spiny neuron (NeuN+/DARPP32+), and nonneuronal populations (NeuN−) were isolated by flow cytometry. The sorting gates are indicated.

(C) ^{14}C concentrations in genomic DNA from striatal medium spiny neuron nuclei (NeuN+/DARPP32+) are not significantly different from atmospheric ^{14}C concentrations at birth for the vast majority of the analyzed individuals.

(D) The ^{14}C concentration in genomic DNA from striatal interneurons corresponds to time points after the birth of most individuals, demonstrating interneuron renewal throughout life. Error bars indicate two standard deviations in ^{14}C concentration in the respective DNA sample.

See also Figure S4 and Table S6.

sufficient to redirect growing axons and develop new circuitry in experimental animals, suggesting that rather small genetic changes can underlie brain evolution (Feldheim et al., 1998). It is conceivable that differential expression of a limited number of guidance molecules may result in rerouting of neuroblasts and integration of neurons in two different and functionally distinct brain regions.

Another major difference between rodents and humans may be the neuronal subtypes generated in the subventricular zone. Calretinin-expressing interneurons are much rarer in rodents, constituting less than 1% of striatal neurons, compared to humans, in whom 10% of striatal interneurons are calretinin positive. The function of this neuronal subclass is essentially unknown, to a large extent due to its paucity in animals amenable to experimental manipulation. Similar to their human counterpart, rodent calretinin-positive interneurons are of medium size and aspiny. However, only a very limited description of their axonal arborization is available and their electrophysiological profile remains unknown (Tepper and Bolam, 2004).

The depletion of adult-born neurons in Huntington's disease may be due to reduced generation of neurons and/or preferential degeneration of adult-born neurons. Huntington's disease is thought to be the result of both loss of function of the normal Huntingtin protein and toxic effects of the modified protein (Zuccato et al., 2010). Huntingtin has been implicated in both embryonic and adult neurogenesis (Ben M'Barek et al., 2013; Godin et al., 2010), and it is possible that failing striatal neurogenesis contributes to the depletion of adult generated neurons. However, since the subjects with early stage disease showed a more modest depletion of adult-born neurons than at the advanced stages (Figure 7), adult-born neurons may be lost with progression of the disease, although the number of subjects available for analysis was limited.

We can currently only speculate about the potential function of continuous striatal neurogenesis in humans, and the functional integration of the new neurons into existing neuronal circuits as well as their effects remain to be investigated. The striatum was first associated with motor control, but it is today well-established that this region also is important for many cognitive

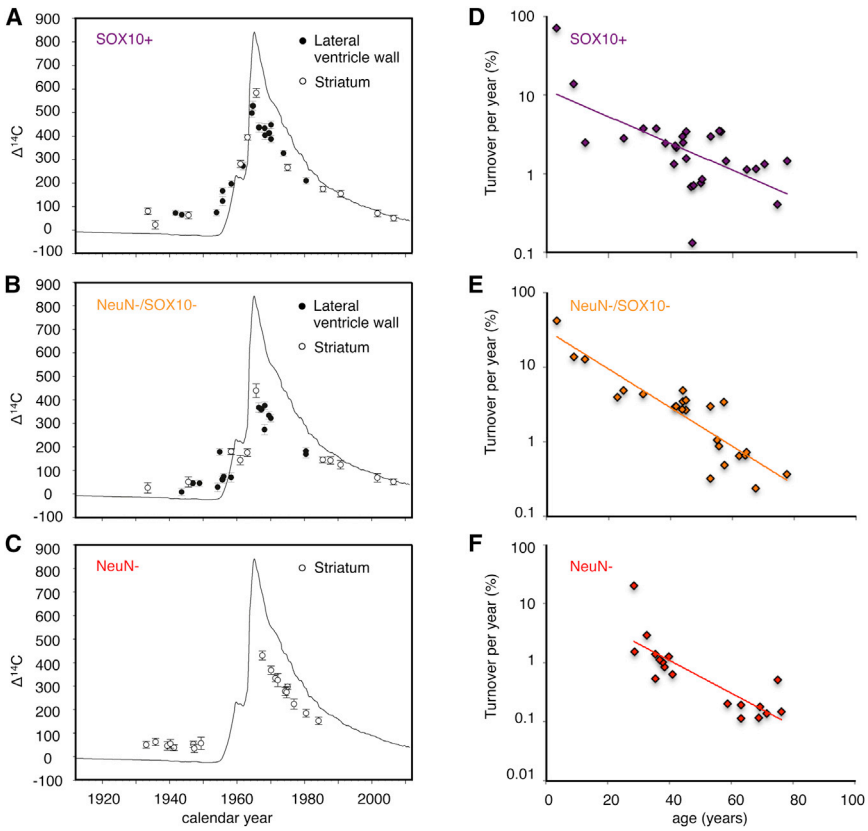

Figure 6. Turnover of Nonneuronal Cells in the Striatum

(A–C) The ^{14}C concentration in genomic DNA from oligodendrocyte lineage cells (SOX10+) (A), from nonneuronal/nonoligodendrocyte lineage cells (NeuN-/SOX10−) (B), and from all nonneuronal cells (NeuN−) (C), corresponds to time points well after the birth of each individual in the lateral ventricle wall (black dots) and in the striatum (white dots).

(D–F) Individual turnover rates for oligodendrocyte lineage cells (D), nonneuronal/ nonoligodendrocyte lineage cells (E), and all nonneuronal cells (F) computed on the basis of individual data fitting. Individual turnover rates are sensitive to deviations in measured ^{14}C and values <0.001 (n = 2) were excluded from the plots, but the full data are given in Table S5. All individual turnover rates estimates are based on the 2POP scenario.

Error bars in (A)–(C) indicate two standard deviations in ^{14}C concentration in the respective DNA sample. See also Figure S5 and Table S6.

functions. Huntington's disease results in motor, cognitive and psychiatric symptoms, with the motor symptoms often being preceded by cognitive impairment. The selective depletion of adult-generated neurons in Huntington's disease indicates that the effect of losing such neurons may be found within the symptoms that these patients display. However, medium spiny neurons account for most of the neuronal loss, and most of the symptomatology is likely explained by this.

The finding that neurons are continuously added in the adult human striatum poses the question of whether this process can be utilized therapeutically in neurological disease. The presence of increased numbers of putative neuroblasts in the human striatum after stroke may indicate increased neurogenesis in this situation (Macas et al., 2006), similarly to what is seen in other mammals. It will be important to study whether such neuroblasts give rise to mature neurons. Increasing the generation or promoting the survival of new neurons is an interesting option in stroke. Moreover, studies in rodents have suggested that promoting cell proliferation in the subventricular zone can have a positive effect in models of Parkinson's disease, likely mediated by the new cells having a neurotrophic effect on the nigro-striatal system (Androutsellis-Theotokis et al., 2009; Zachrisson et al., 2011). Investigating how striatal neurogenesis is potentially affected in pathological situations and identifying factors that promote the renewal of striatal neurons may facilitate the development of therapeutic strategies to improve functional recovery after injury or to tackle neurodegenerative disorders.

EXPERIMENTAL PROCEDURES

Tissue Collection

After informed consent from the relatives was given, tissues were obtained from cases admitted between 1991 and 2013 to the Swedish National Department of Forensic Medicine for autopsy, the NICHD Brain and Tissue Bank from the University of Maryland (US), and the Cambridge Brain Bank (UK). Ethical permission for this study was granted by Regional Ethics Committee of Sweden (No 02-418, 2005/185, 2006/1029-31/2, 2006/189-31, 2010-313/31-3) and the institutional review boards of the University of Maryland and Cambridge University. Lateral wall of the lateral ventricle or striatum (caudate nucleus including the lateral wall of the lateral ventricle, putamen and internal capsule) were dissected. Cerebellum and occipital cortex samples served as controls. Brain tissue was frozen and stored at −80°C until analysis. Formalin-fixed and paraffin-embedded sections of the striatum, hippocampus, and cortex were obtained from cancer patients who received IdU infusion as a radiosensitizer for therapeutic purposes at the National Heart, Lung and Blood Institute, National Institutes of Health, Bethesda, US. Additionally, olfactory bulbs from donors who did not receive IdU were examined.

Nuclei Isolation

Tissue samples were thawed and Dounce homogenized in 10 ml lysis buffer (0.32 M sucrose, 5 mM $CaCl_2$, 3 mM magnesium acetate, 0.1 mM EDTA, 10 mM Tris-HCl [pH 8.0], 0.1% Triton X-100, 1 mM DTT). Homogenized samples were suspended in 20 ml of sucrose solution (1.8 M sucrose, 3 mM magnesium acetate, 1 mM DTT, and 10 mM Tris-HCl [pH 8.0]), layered onto a cushion of 10 ml sucrose solution, and centrifuged at 36,500 × g for 2.4 hr at 4°C. The isolated nuclei were resuspended in nuclei storage buffer (10 mMTris [pH = 7.2], 2 mM $MgCl_2$, 70 mM KCl, 15% sucrose) for immunostaining and flow cytometry analysis.

FACS Sorting and Analysis

Isolated nuclei were stained sequentially with mouse NeuN (A-60) (Millipore, 1:800) and either rabbit DARPP32 (Cell signaling, 1:200) or goat SOX10 (R&D, 1:300). NeuN (A-60) antibody was directly conjugated to Alexa 647 (Alexa Fluor 647 Antibody Labeling Kit, Invitrogen) and DARPP32 antibody was directly conjugated to Alexa 488 (Cell signaling). Secondary antibody conjugated to Alexa 488 (Invitrogen, 1:500) was used to detect SOX10. Flow cytometry analyses and sorting were performed with a BD FACS Influx

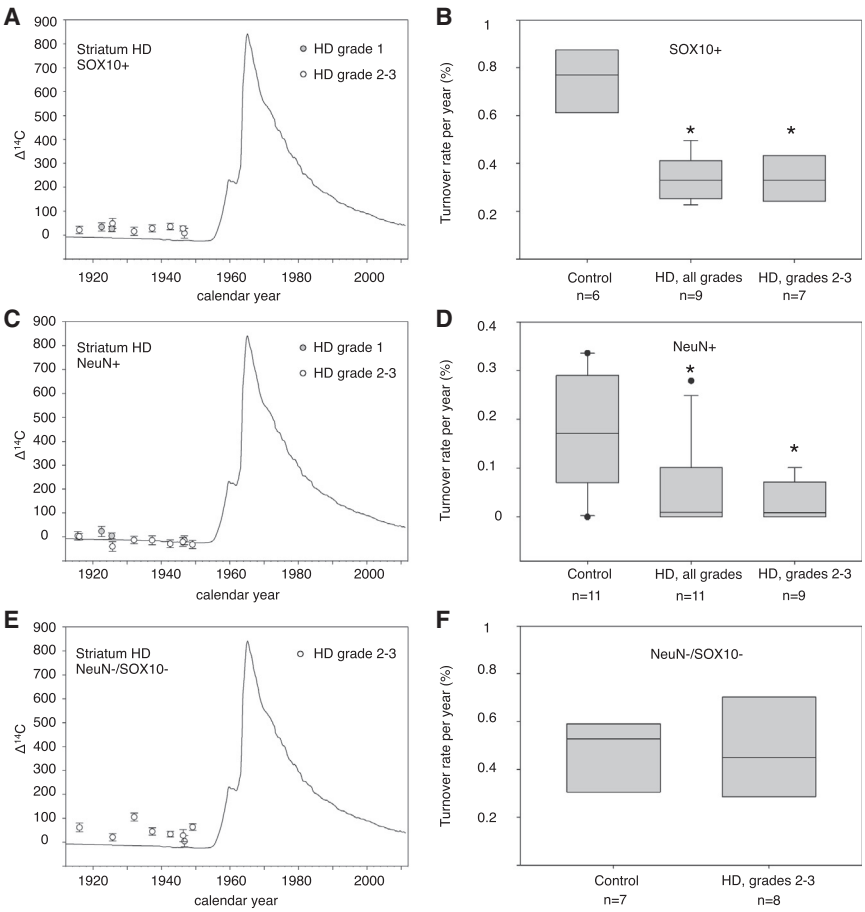

Figure 7. Cell Turnover in the Striatum of Huntington's Disease Patients

(A–F) Cell turnover in the striatum of patients affected by Huntington's disease. Grey dots indicate individually measured ^{14}C concentrations in the genomic DNA of nuclei isolated from the striatum of individuals with grade 1 Huntington's disease. White dots show ^{14}C concentrations in the genomic DNA of striatal nuclei from individuals with grade 2 or grade 3 Huntington's disease. The ^{14}C concentration in genomic DNA from oligodendrocyte lineage cells, defined by SOX10 expression, corresponds to time points after the birth of each individual (A). The individual turnover rates from oligodendrocyte lineage cells are significantly lower in individuals with Huntington's disease (HD) compared to age-matched nonaffected subjects (B). ^{14}C concentrations in genomic DNA from neuronal nuclei isolated from the striatum of individuals with grade 1 Huntington's disease are slightly above atmospheric ^{14}C concentrations at birth, whereas ^{14}C concentrations in genomic DNA from neuronal nuclei isolated from the striatum of individuals with grade 2 or 3 Huntington's disease are not significantly different from atmospheric ^{14}C concentrations at birth (C). The individual turnover rates from striatal neurons are significantly lower in individuals with Huntington's disease compared to nonaffected age-matched controls (D). The ^{14}C concentrations of genomic DNA from nonneuronal/non-oligodendrocyte lineage cells, defined by the absence of NeuN and SOX10 labeling, demonstrate postnatal cell turnover in the striatum of patients affected by Huntington's disease (E). The individual turnover rates from nonneuronal/non-oligodendrocyte lineage cells do not significantly differ between individuals with Huntington's disease and nonaffected subjects (F). *$p < 0.05$, Mann-Whitney test for equal medians. Individual turnover rate estimations are based on scenario A (see Extended Experimental Procedures) to allow comparing healthy subjects with Huntington's disease patients in spite of the difference in the respective renewing fractions. This results in an underestimation of the turnover rate in the healthy donors compared to the turnover rate in the renewing fraction (scenario 2POP). Error bars in (A), (C), and (E) indicate two standard deviations in ^{14}C concentration in the respective DNA sample. See also Table S6.

sorter (BD Biosciences). The FACS gating strategies for sorts are shown in Figures 4 and 5.

Summary of the Mathematical Modeling

Mathematical modeling was based on birth-and-death processes representing different lifetime scenarios, as described (Bergmann et al., 2009; Spalding et al., 2013) and as outlined in detail in the Extended Experimental Procedures. These models were integrated along the atmospheric ^{14}C curve to yield a predicted DNA ^{14}C concentration. Nonlinear least-square and Monte Carlo Markov chain methods were used to estimate the best global parameters for each scenario, for the neuronal and the nonneuronal cell samples. The small-sample-corrected Akaike Information Criterion (AICc) was used to rank the different scenarios. Individual turnover rates were estimated from Scenarios A and 2POP, for all the samples. Scenario A provided a direct turnover rate estimate for each sample. However, for Scenario 2POP, fixed fractions of renewing were set based on the best fit for the global parameter estimates.

SUPPLEMENTAL INFORMATION

Supplemental Information includes Extended Experimental Procedures, five figures, and seven tables and can be found with this article online at http://dx.doi.org/10.1016/j.cell.2014.01.044.

ACKNOWLEDGMENTS

We thank the Cambridge Brain Bank, Cambridge (UK), and the NICHD Brain and Tissue Bank for Developmental Disorders, Baltimore, Maryland (USA), for providing tissue. The Cambridge Brain Bank is supported by the NIHR Cambridge Biomedical Research Centre. The staff at the Swedish National Board of Forensic Medicine is acknowledged for cooperation in tissue donation. We thank Marcelo Toro, Sarantis Giatrellis, and Mathilde Chapuis for help with flow cytometry and evaluation of immunostainings and Helena Lönnqvist for help with DNA extraction. We thank Nenad Bogdanovic for anatomical evaluation of human brain sections, Konstantinos Meletis for discussions, and Karl Håkansson for AMS samples preparation. This study was supported by grants from the Swedish Research Council, the Swedish Cancer Society, the Karolinska Institute, Tobias Stiftelsen, AFA Försäkringar, the Strategic Research Programme in Stem Cells and Regenerative Medicine at Karolinska Institutet (StratRegen), the ERC and Knut och Alice Wallenbergs Stiftelse, the regional agreement on medical training and clinical research between Stockholm County Council and the Karolinska Institutet (ALF 20080508) and Torsten Söderbergs Stiftelse.

Received: October 15, 2013
Revised: November 29, 2013
Accepted: January 20, 2014
Published: February 20, 2014

REFERENCES

Androutsellis-Theotokis, A., Rueger, M.A., Park, D.M., Mkhikian, H., Korb, E., Poser, S.W., Walbridge, S., Munasinghe, J., Koretsky, A.P., Lonser, R.R., and McKay, R.D. (2009). Targeting neural precursors in the adult brain rescues injured dopamine neurons. Proc. Natl. Acad. Sci. USA *106*, 13570–13575.

Arvidsson, A., Collin, T., Kirik, D., Kokaia, Z., and Lindvall, O. (2002). Neuronal replacement from endogenous precursors in the adult brain after stroke. Nat. Med. *8*, 963–970.

Bédard, A., Cossette, M., Lévesque, M., and Parent, A. (2002a). Proliferating cells can differentiate into neurons in the striatum of normal adult monkey. Neurosci. Lett. *328*, 213–216.

Bédard, A., Lévesque, M., Bernier, P.J., and Parent, A. (2002b). The rostral migratory stream in adult squirrel monkeys: contribution of new neurons to the olfactory tubercle and involvement of the antiapoptotic protein Bcl-2. Eur. J. Neurosci. *16*, 1917–1924.

Ben M'Barek, K., Pla, P., Orvoen, S., Benstaali, C., Godin, J.D., Gardier, A.M., Saudou, F., David, D.J., and Humbert, S. (2013). Huntingtin mediates anxiety/depression-related behaviors and hippocampal neurogenesis. J. Neurosci. *33*, 8608–8620.

Bergmann, O., Bhardwaj, R.D., Bernard, S., Zdunek, S., Barnabé-Heider, F., Walsh, S., Zupicich, J., Alkass, K., Buchholz, B.A., Druid, H., et al. (2009). Evidence for cardiomyocyte renewal in humans. Science *324*, 98–102.

Bergmann, O., Liebl, J., Bernard, S., Alkass, K., Yeung, M.S., Steier, P., Kutschera, W., Johnson, L., Landén, M., Druid, H., et al. (2012). The age of olfactory bulb neurons in humans. Neuron *74*, 634–639.

Bhardwaj, R.D., Curtis, M.A., Spalding, K.L., Buchholz, B.A., Fink, D., Björk-Eriksson, T., Nordborg, C., Gage, F.H., Druid, H., Eriksson, P.S., and Frisén, J. (2006). Neocortical neurogenesis in humans is restricted to development. Proc. Natl. Acad. Sci. USA *103*, 12564–12568.

Cicchetti, F., Prensa, L., Wu, Y., and Parent, A. (2000). Chemical anatomy of striatal interneurons in normal individuals and in patients with Huntington's disease. Brain Res. Brain Res. Rev. *34*, 80–101.

Clelland, C.D., Choi, M., Romberg, C., Clemenson, G.D., Jr., Fragniere, A., Tyers, P., Jessberger, S., Saksida, L.M., Barker, R.A., Gage, F.H., and Bussey, T.J. (2009). A functional role for adult hippocampal neurogenesis in spatial pattern separation. Science *325*, 210–213.

Curtis, M.A., Penney, E.B., Pearson, A.G., van Roon-Mom, W.M., Butterworth, N.J., Dragunow, M., Connor, B., and Faull, R.L. (2003). Increased cell proliferation and neurogenesis in the adult human Huntington's disease brain. Proc. Natl. Acad. Sci. USA *100*, 9023–9027.

Dayer, A.G., Cleaver, K.M., Abouantoun, T., and Cameron, H.A. (2005). New GABAergic interneurons in the adult neocortex and striatum are generated from different precursors. J. Cell Biol. *168*, 415–427.

Eisch, A.J., and Petrik, D. (2012). Depression and hippocampal neurogenesis: a road to remission? Science *338*, 72–75.

Eriksson, P.S., Perfilieva, E., Björk-Eriksson, T., Alborn, A.M., Nordborg, C., Peterson, D.A., and Gage, F.H. (1998). Neurogenesis in the adult human hippocampus. Nat. Med. *4*, 1313–1317.

Feldheim, D.A., Vanderhaeghen, P., Hansen, M.J., Frisén, J., Lu, Q., Barbacid, M., and Flanagan, J.G. (1998). Topographic guidance labels in a sensory projection to the forebrain. Neuron *21*, 1303–1313.

Ge, S., Yang, C.H., Hsu, K.S., Ming, G.L., and Song, H. (2007). A critical period for enhanced synaptic plasticity in newly generated neurons of the adult brain. Neuron *54*, 559–566.

Godin, J.D., Colombo, K., Molina-Calavita, M., Keryer, G., Zala, D., Charrin, B.C., Dietrich, P., Volvert, M.L., Guillemot, F., Dragatsis, I., et al. (2010). Huntingtin is required for mitotic spindle orientation and mammalian neurogenesis. Neuron *67*, 392–406.

Göritz, C., and Frisén, J. (2012). Neural stem cells and neurogenesis in the adult. Cell Stem Cell *10*, 657–659.

Hou, S.W., Wang, Y.Q., Xu, M., Shen, D.H., Wang, J.J., Huang, F., Yu, Z., and Sun, F.Y. (2008). Functional integration of newly generated neurons into striatum after cerebral ischemia in the adult rat brain. Stroke *39*, 2837–2844.

Kang, H.J., Kawasawa, Y.I., Cheng, F., Zhu, Y., Xu, X., Li, M., Sousa, A.M., Pletikos, M., Meyer, K.A., Sedmak, G., et al. (2011). Spatio-temporal transcriptome of the human brain. Nature *478*, 483–489.

Kempermann, G. (2012). New neurons for 'survival of the fittest'. Nat. Rev. Neurosci. *13*, 727–736.

Kheirbek, M.A., Klemenhagen, K.C., Sahay, A., and Hen, R. (2012). Neurogenesis and generalization: a new approach to stratify and treat anxiety disorders. Nat. Neurosci. *15*, 1613–1620.

Klempin, F., Kronenberg, G., Cheung, G., Kettenmann, H., and Kempermann, G. (2011). Properties of doublecortin-(DCX)-expressing cells in the piriform cortex compared to the neurogenic dentate gyrus of adult mice. PLoS ONE *6*, e25760.

Knoth, R., Singec, I., Ditter, M., Pantazis, G., Capetian, P., Meyer, R.P., Horvat, V., Volk, B., and Kempermann, G. (2010). Murine features of neurogenesis in the human hippocampus across the lifespan from 0 to 100 years. PLoS ONE *5*, e8809.

Kohl, Z., Regensburger, M., Aigner, R., Kandasamy, M., Winner, B., Aigner, L., and Winkler, J. (2010). Impaired adult olfactory bulb neurogenesis in the R6/2 mouse model of Huntington's disease. BMC Neurosci. *11*, 114.

Kohler, S.J., Williams, N.I., Stanton, G.B., Cameron, J.L., and Greenough, W.T. (2011). Maturation time of new granule cells in the dentate gyrus of adult macaque monkeys exceeds six months. Proc. Natl. Acad. Sci. USA *108*, 10326–10331.

Luzzati, F., De Marchis, S., Fasolo, A., and Peretto, P. (2006). Neurogenesis in the caudate nucleus of the adult rabbit. J. Neurosci. *26*, 609–621.

Macas, J., Nern, C., Plate, K.H., and Momma, S. (2006). Increased generation of neuronal progenitors after ischemic injury in the aged adult human forebrain. J. Neurosci. *26*, 13114–13119.

Miller, S.A., Dykes, D.D., and Polesky, H.F. (1988). A simple salting out procedure for extracting DNA from human nucleated cells. Nucleic Acids Res. *16*, 1215.

Nacher, J., Alonso-Llosa, G., Rosell, D., and McEwen, B. (2002). PSA-NCAM expression in the piriform cortex of the adult rat. Modulation by NMDA receptor antagonist administration. Brain Res. *927*, 111–121.

Nakashiba, T., Cushman, J.D., Pelkey, K.A., Renaudineau, S., Buhl, D.L., McHugh, T.J., Rodriguez Barrera, V., Chittajallu, R., Iwamoto, K.S., McBain, C.J., et al. (2012). Young dentate granule cells mediate pattern separation, whereas old granule cells facilitate pattern completion. Cell *149*, 188–201.

Plümpe, T., Ehninger, D., Steiner, B., Klempin, F., Jessberger, S., Brandt, M., Römer, B., Rodriguez, G.R., Kronenberg, G., and Kempermann, G. (2006). Variability of doublecortin-associated dendrite maturation in adult hippocampal neurogenesis is independent of the regulation of precursor cell proliferation. BMC Neurosci. *7*, 77.

Rakic, P. (1985). Limits of neurogenesis in primates. Science *227*, 1054–1056.

Ransome, M.I., Renoir, T., and Hannan, A.J. (2012). Hippocampal neurogenesis, cognitive deficits and affective disorder in Huntington's disease. Neural Plast. *2012*, 874387.

Sahay, A., Scobie, K.N., Hill, A.S., O'Carroll, C.M., Kheirbek, M.A., Burghardt, N.S., Fenton, A.A., Dranovsky, A., and Hen, R. (2011). Increasing adult hippocampal neurogenesis is sufficient to improve pattern separation. Nature *472*, 466–470.

Salehpour, M., Hakansson, K., and Possnert, G. (2013a). Accelerator mass spectrometry of ultra-small samples with applications in the biosciences. Nucl Instrum Methods Phys Res B *294*, 97–103.

Salehpour, M., Håkansson, K., Possnert, G., Westermark, P., Antoni, G., and Wikström, G. (2013b). Life Science Applications Utilizing Radiocarbon Tracing. Radiocarbon *55*, 865–873.

Sanai, N., Nguyen, T., Ihrie, R.A., Mirzadeh, Z., Tsai, H.H., Wong, M., Gupta, N., Berger, M.S., Huang, E., Garcia-Verdugo, J.M., et al. (2011). Corridors of

migrating neurons in the human brain and their decline during infancy. Nature *478*, 382–386.

Schmidt-Hieber, C., Jonas, P., and Bischofberger, J. (2004). Enhanced synaptic plasticity in newly generated granule cells of the adult hippocampus. Nature *429*, 184–187.

Seki, T. (2002). Expression patterns of immature neuronal markers PSA-NCAM, CRMP-4 and NeuroD in the hippocampus of young adult and aged rodents. J. Neurosci. Res. *70*, 327–334.

Spalding, K.L., Bhardwaj, R.D., Buchholz, B.A., Druid, H., and Frisén, J. (2005). Retrospective birth dating of cells in humans. Cell *122*, 133–143.

Spalding, K.L., Bergmann, O., Alkass, K., Bernard, S., Salehpour, M., Huttner, H.B., Boström, E., Westerlund, I., Vial, C., Buchholz, B.A., et al. (2013). Dynamics of hippocampal neurogenesis in adult humans. Cell *153*, 1219–1227.

Sulzer, D., Mosharov, E., Talloczy, Z., Zucca, F.A., Simon, J.D., and Zecca, L. (2008). Neuronal pigmented autophagic vacuoles: lipofuscin, neuromelanin, and ceroid as macroautophagic responses during aging and disease. J. Neurochem. *106*, 24–36.

Tepper, J.M., and Bolam, J.P. (2004). Functional diversity and specificity of neostriatal interneurons. Curr. Opin. Neurobiol. *14*, 685–692.

Tonchev, A.B., Yamashima, T., Zhao, L., Okano, H.J., and Okano, H. (2003). Proliferation of neural and neuronal progenitors after global brain ischemia in young adult macaque monkeys. Mol. Cell. Neurosci. *23*, 292–301.

Tonchev, A.B., Yamashima, T., Sawamoto, K., and Okano, H. (2005). Enhanced proliferation of progenitor cells in the subventricular zone and limited neuronal production in the striatum and neocortex of adult macaque monkeys after global cerebral ischemia. J. Neurosci. Res. *81*, 776–788.

Tong, J., Furukawa, Y., Sherwin, A., Hornykiewicz, O., and Kish, S.J. (2011). Heterogeneous intrastriatal pattern of proteins regulating axon growth in normal adult human brain. Neurobiol. Dis. *41*, 458–468.

Walker, F.O. (2007). Huntington's disease. Lancet *369*, 218–228.

Walker, T.L., Turnbull, G.W., Mackay, E.W., Hannan, A.J., and Bartlett, P.F. (2011). The latent stem cell population is retained in the hippocampus of transgenic Huntington's disease mice but not wild-type mice. PLoS ONE *6*, e18153.

Wang, C., Liu, F., Liu, Y.Y., Zhao, C.H., You, Y., Wang, L., Zhang, J., Wei, B., Ma, T., Zhang, Q., et al. (2011). Identification and characterization of neuroblasts in the subventricular zone and rostral migratory stream of the adult human brain. Cell Res. *21*, 1534–1550.

Wei, B., Nie, Y., Li, X., Wang, C., Ma, T., Huang, Z., Tian, M., Sun, C., Cai, Y., You, Y., et al. (2011). Emx1-expressing neural stem cells in the subventricular zone give rise to new interneurons in the ischemic injured striatum. Eur. J. Neurosci. *33*, 819–830.

Zachrisson, O., Zhao, M., Andersson, A., Dannaeus, K., Häggblad, J., Isacson, R., Nielsen, E., Patrone, C., Rönnholm, H., Wikström, L., et al. (2011). Restorative Effects of Platelet DerivedGrowth Factor-BB in Rodent Modelsof Parkinson's Disease. J. Parkinsons's Dis. *1*, 49–63.

Zuccato, C., Valenza, M., and Cattaneo, E. (2010). Molecular mechanisms and potential therapeutical targets in Huntington's disease. Physiol. Rev. *90*, 905–981.

EXTENDED EXPERIMENTAL PROCEDURES

Immunohistochemistry

Frozen sections (10–20 μm) were prepared with a cryostat (HM500 M, Microm) and fixed in 2% formaldehyde in PBS for 10 min. Sections were blocked (10% donkey normal serum in PBS with 0.2% Triton X-100) at room temperature for 1hr and incubated with the respective primary antibody: mouse NeuN (Millipore A-60 clone; 1:100), rabbit Fox3 (Atlas Antibody, 1:300), mouse GFAP (direct conjugated to Cy3, clone G-A-5, Sigma, 1:2,000), rabbit GFAP (Dako, 1:2,000), rabbit cleaved Caspase-3 (Cell Signaling, 1:500), goat Sox10 (R&D, 1:500), chicken MAP-2 (Abcam, 1:1,000), rabbit calretinin (Atlas antibody, 1:100), mouse calretinin (Dako, 1:50), rabbit parvalbumin (Abcam, 1:1,000), rabbit CNPase (Atlas Antibody, 1:400), mouse HuD/HuC 16A11-biotin (Invitrogen, 1:100), goat DCX (Santa Cruz, 1:200), guinea pig DCX (Millipore, 1:500), mouse PSA-NCAM (Millipore, 1:400), UEA1 (direct conjugated to Alexa 488, Vector, 1:500), rabbit DARPP32 (direct conjugated to Alexa 488, Cell signaling, 1:100), goat ChAT (Millipore, 1:100), rabbit NPY (Sigma, 1:1,000) and visualized with the matching secondary antibody and streptavidin conjugated to Alexa 488, Cy3, or Alexa 647 (1:500, Invitrogen). Antiautofluorescence treatment was applied when necessary (Immunoclear, Be Immunoclear, Stockholm, Sweden). Cell nuclei were visualized with DAPI. Pictures were taken using a Zeiss LSM700 confocal microscope with the Zen software. Image processing and assembly were performed in ImageJ and Photoshop.

Lipofuscin Quantification

Lipofuscin granules were located by confocal fluorescence microscopy and counted from digital images in caudate nucleus sections from three subjects for the analysis of lipofuscin content in the different striatal neuronal subtypes (age 21–26), from three subjects for the analysis in the adult dentate gyrus, from six subjects for the analysis in the pediatric striatum, and from three subjects for the analysis in the striatum in Huntington's disease. Cells that were not entirely contained in the section were not counted to avoid missing lipofuscin granules.

Immunofluorescent Detection of Iododeoxyuridine

Samples of the striatum, hippocampus and cortex were obtained from cancer patients who received IdU infusion as a radiosensitizer for therapeutic purposes. Additionally, olfactory bulbs from patients who did not receive IdU were examined. Detection of IdU in formalin fixed paraffin-embedded sections was done according to a protocol adapted from a previous study (Tuttle et al., 2010). Briefly, paraffin was removed by immersing slides in xylene and tissue was rehydrated by passing through a descending ethanol series. Sections were permeabilized with 0.2% Triton X-100 and antigen retrieval was done in citraconic acid solution (pH = 7.4; 0.05% citraconic acid) for 20 min in a domestic steamer. The sections were allowed to cool down for 20 min and immersed in 1.5 N HCl for 40 min at room temperature. Sections were blocked (10% donkey normal serum in PBS with 0.2% Triton X-100) at room temperature for 1h and then incubated with the respective primary antibody: mouse BrdU (BD, clone B44, 1:60), rabbit Fox3 (Atlas antibody, 1:80), chick MAP2 (abcam, 1:400) or rabbit calretinin (Atlas antibody, 1:100) and visualized with the matching secondary antibody conjugated to Cy3, Alexa 488, or Alexa 647 (1:500, Invitrogen). When necessary, sudan black (0.1% in 70% ethanol) was applied for 10 min at room temperature to decrease autofluorescence. IdU staining was not detected in the brains of subjects not exposed to IdU.

DNA Purification

DNA purification was carried out in a clean room (ISO8) to avoid any carbon contamination of the samples. All glassware was prebaked at 450°C for more than 4 hr. DNA isolation was performed according to a modified protocol (Miller et al., 1988). Briefly, 500 μl DNA lysis buffer (100 mM Tris [pH 8.0], 200 mM NaCl, 1% SDS, and 5 mM EDTA) and 6 μl Proteinase K (20 mg/ml) were added to the collected nuclei and incubated overnight at 65°C. RNase cocktail was added (Ambion) and samples were incubated at 65°C for 1 hr. Half of the existing volume of 5 M NaCl solution was added, and the mixture was agitated for 15 s. The solution was spun down at 13,000 rpm for 3 min. The supernatant containing the DNA was transferred to a 12 ml glass vial. Then, 3 volumes of absolute ethanol were added and the glass vial was inverted several times to precipitate the DNA. The DNA precipitate was washed three times in DNA-washing solution (70% ethanol [v/v] and 0.1 M NaCl) and transferred to 500 μl DNase- and RNase-free water (GIBCO). The DNA was quantified, and DNA purity was verified by UV spectroscopy (NanoDrop).

Accelerator Mass Spectrometry

All accelerator mass spectrometry (AMS) analyses were performed blind to the identity of the sample. Purified DNA samples suspended in water were lyophilized to dryness. To convert the DNA samples into graphite, excess CuO was added to each dry sample, and the tubes were evacuated and sealed with a high-temperature torch. Tubes were placed in a furnace set at 900°C for 3.5 hr to combust all carbon to CO_2. The evolved CO_2 was purified, trapped, and reduced to graphite in the presence of iron catalyst in individual reactors at 550°C for 6 hr. Graphite targets were measured at the Department of Physics and Astronomy, Ion Physics, of Uppsala University (Salehpour et al., 2013a; Salehpour et al., 2013b). Large CO_2 samples (>100 μg) were split, and $\delta^{13}C$ was measured by stable isotope ratio mass spectrometry, which established the $\delta^{13}C$ correction to –22.3‰ ± 0.5‰ (1 SD), which was applied for all samples. The measurement error was determined for each sample and ranged between ± 4‰ and ± 12‰

(1 SD) $\Delta^{14}C$ for the large and small samples (10 μg C), respectively. All ^{14}C data are reported as decay-corrected $\Delta^{14}C$ or fraction modern.

Correction for FACS Impurities

FACS impurities were corrected for by solving the following equation system for $\Delta^{14}C_{non\text{-}neurons\_corrected}$ and $\Delta^{14}C_{neurons\_corrected}$ ($y_{impurity\_non\text{-}neurons}$ and $x_{impurity\_neurons}$ are given in percentages). Corrected values are shown in Table S5.

$$\Delta^{14}C_{non\text{-}neurons\_measured} * 100 = \left(100 - y_{impurity\ non\text{-}neurons}\right) * \Delta^{14}C_{non\text{-}neurons\_corrected} + y_{impurity\_non\text{-}neurons} * \Delta^{14}C_{neurons\_corrected} \quad (1)$$

$$\Delta^{14}C_{neurons\_measured} * 100 = \left(100 - x_{impurity\ neurons}\right) * \Delta^{14}C_{neurons\_corrected} + x_{impurity\_neurons} * \Delta^{14}C_{non\text{-}neurons\_corrected} \quad (2)$$

Gene Expression of Sorted Nuclei

Nuclei isolates were labeled with NeuN and SOX10 antibodies and flow cytometry sorted according to their immunoreactivity. Total RNA was extracted from NeuN-positive, SOX10-positive and double-negative populations, respectively, using the RNeasy mini plus kit (QIAGEN). Equal amounts of total RNA from each sample was reverse transcribed to cDNA using the QuantiTect RT kit (QIAGEN). cDNA concentration was measured using the Quant-iT dsDNA assay high-sensitivity kit (Invitrogen). cDNA from each sample was amplified with TaqMan Universal PCR master mix (Applied Biosystems) and TaqMan gene expression assays (Applied Biosystems). The following TaqMan gene expression assays were used: NeuN (Assay ID: Hs01370653_m1), SOX10 (Assay ID: Hs0036698_m1), GFAP (Assay ID: Hs00909233), CNP (Assay ID: Hs00263981), MAP2 (Assay ID: Hs00258900), 18 s (Assay ID: Hs9999901_s1), CD45 (Assay ID: Hs00894732_m1), PLP1 (Assay ID: Hs00166914_m1). Quantitative real-time PCR was performed with a Fast Real-Time PCR System 7500 (Applied Biosystems). The relative mRNA levels were calculated with the Ct method, using 18 s rRNA to normalize.

Western Blot

Tissue samples of dissected human striatum, hippocampus and cerebellum were lysed in RIPA lysis buffer (50 mM Tris, pH 8, 150 mM NaCl, 10% glycerol, 1% NP-40, 0.5% sodium deoxycholate) supplemented with protease inhibitor cocktail (Roche) and homogenized with a dounce. For immunoblotting, proteins were separated by SDS-PAGE and electrotransferred to PVDF-membranes (Immobilon P, Millipore), which were blocked with 5% milk in Tris-buffered saline with 0.1% Tween 20 and incubated overnight at 4°C with the following primary antibodies: β-actin (1:5,000, mouse, Sigma, A2228), DCX (1:3,000, guinea pig, Millipore), PSA-NCAM (1: 1,000, mouse, Millipore). The primary antibodies were detected with horseradish peroxidase-conjugated secondary antibodies and an ECL detection system (GE Healthcare).

Mathemetical Modeling

Models for Cell Renewal

Integration of atmospheric ^{14}C derived from nuclear testing in replicating DNA offers the possibility to quantify the amount of cell renewal over periods ranging from few years to decades. We used a set of cell birth-and-death models to explore the renewal dynamics of different cell types. For a given model, we computed the values of the birth-and-death parameters that fitted best to the data.

Birth-and-Death Model

Birth-and-death models describe the dynamics (the evolution in time) of a cell population in an individual, in which cells can either be born or die. In an individual aged t years, we denote by $N(t)$ the *cell number* in the cell population. Keeping in mind that the atmospheric ^{14}C data provide information on the birth-date of the cells, we also want to track the chronological age of each cell. The chronological age of a cell is defined as the time elapsed since its last division. To take into account the age of the cells, we brake down the population $N(t)$ into a continuum of age bins. We say that the population is structured in chronological cell age a. The new dynamical variable $n(t,a)$ is the *cell density* at age a at time t. The *cell number* and the *cell density* are related in the following way

$$N(t) = \int_0^\infty n(t,a)da.$$

The cell density is expressed in *cells per year*, reflecting the fact that, for a small age bin Δa years, the number of cells aged between a and $a + \Delta a$ is approximately n(t,a) × Δa cells.

To fully specify the model, we will make the following modeling hypotheses.

H1 Time- and Age-Dependent Cell Death Rate. The cell *death rate* γ (units: per year) depends on the age of the individual t and the age of the cell a: $\gamma = \gamma(t,a)$. The death rate does not depend on the state of the cell population.

H2 All Cells Initially Aged 0 at Time t_0 before Birth. Individuals develop N_0 cells at a time t_0 before their birth, all of them are assumed to be of age $a = 0$. This assumption implies that $a \in [0, t + t_0]$ (cells are younger than or as old as the individual). Cells formed prenatally are set an age 0 at birth. To simplify the rest of the presentation, we will reset the age of the individual from $t \to t + t_0$, i.e., the time since

the beginning of actual development instead of birth. In practice, birth dates of individuals are shifted by an amount t_0, to give the calendar date of the beginning of development $D_{dev} = D_{birth} - t_0$.

H3 Time-Dependent Birth Rate. During the lifetime of an individual, the cell *birth rate* β depends on the age of the individual t: $\beta = \beta(t)$. The birth rate does not depend on the state of the cell population.

The equations for the evolution of the cell density are

$$\text{(PDE)} \qquad \underbrace{\frac{\partial n(t,a)}{\partial a}}_{\text{change in person age}} + \underbrace{\frac{\partial n(t,a)}{\partial a}}_{\text{change in cell age}} = \underbrace{-\gamma(t,a)n(t,a)}_{\text{loss of cells}},$$

$$\text{(Initial Condition)} \qquad n(t=0,a) = \underbrace{N_0\delta(a)}_{\substack{\text{all cells aged 0}\\ \text{at start of development}}},$$

$$\text{(Boundary Condition)} \qquad \underbrace{n(t,a=0)}_{\text{newborns}} = \underbrace{\beta(t)}_{\text{cell birth}} \quad \text{for } t \in [0, t_{death}].$$

The first equation is a linear partial differential equation (PDE) that is often used in population dynamics (Perthame, 2007). It is a biological transport equation, with the term transport used in the sense that cells are transported along their age at a unit speed (i.e., they get older). The negative sign on the right-hand-side of the PDE indicates cell loss due to death (H1). The initial condition states that cells are initially aged 0 (H2). The Dirac delta-function δ takes a value zero when a is not 0, and is normalized so that the total cell number

$$\int_0^\infty N_0\delta(a)da = N_0.$$

According to the PDE, cells can only die but no source term for new cell is provided. We need to supplement the PDE with a special condition for newborn cells. The boundary condition specifies the birth rate of the cells ($n(t, a = 0)$) (H3). The equations are valid on domain $a \in [0, t]$, and $t \in [0, t_{death}]$, where t_{death} = *age at death* + t_0.

Hypothesis H1 and H3 exclude the possibility to take into account homeostatic feedback regulation mechanisms, such as repair, which would depend on the balance of different cell type numbers.

In addition to these three modeling hypotheses, we considered several sets of additional hypotheses. Each set of hypotheses is referred to as a scenario. A scenario provides testable hypotheses on how cells are born and die. Each scenario is described by a set of parameters that will be estimated from experimental data.

Scenarios

A (1 Parameter: r). The death rate $\gamma(t,a)$ is constant and the cell number $N(t)$ is constant. In this scenario, the death rate corresponds to the instantaneous proportion of cells renewed, and is termed *turnover rate*.

Death rate: $\gamma(t,a) = r$ constant.

Birth rate: $\beta(t) = N_0 r$.

B (2 Parameters: r, b). The death rate $\gamma(t,a)$ is constant and the birth rate $\beta(t)$ is constant, but independent from the death rate. In particular, the cell number $N(t)$ increases or decreases with time when birth and death rates are different.

Death rate: $\gamma(t,a) = r$ constant.

Birth rate: $\beta(t) = N_0 b$ constant.

C (2 Parameters: r, θ). The death rate is decreasing with the age of the subject $\gamma(t,a) = \gamma(t)$ is a decreasing function. The cell number $N(t)$ is constant.

Death rate:

$$\gamma(t,a) = \gamma(t) = \begin{cases} r & t \le \theta, \\ 0 & t > \theta. \end{cases}$$

$$\text{Birth rate} : \beta(t) = N_0\gamma(t).$$

E (2 Parameters: r, θ). The death rate decreases with cell age a: $\gamma(t,a) = \gamma(a)$. The cell number $N(t)$ is constant.

Death rate:

$$\gamma(t,a) = \gamma(a) = r\frac{\theta}{\theta + a}.$$

Birth rate: The birth rate is obtained by solving a Volterra equation (also called renewal equation):

$$\underbrace{\beta(t)/N_0}_{\text{rate of new cells needed}} = \underbrace{\gamma(t)exp\left(-\int_0^t \gamma(s)ds\right)}_{\text{cells from development dying at time } t} + \underbrace{\int_0^t \beta(t-a)\gamma(a)exp\left(-\int_0^a \gamma(s)ds\right)da}_{\text{cells born } a \text{ years ago, dying at time } t}.$$

2POP (2 Parameters: r, f). The population consists of two populations, one renewing and one not renewing. The renewing fraction follows scenario A.

Death rate: $\gamma(t,a) = r$ constant.

Birth rate: $\beta(t) = N_0 r$.

Fraction of renewing subset: f constant.

XPOP (3 Parameters, r, θ, h). The population consists of a continuum of renewing populations, each with a different turnover rate. The three parameters determine the turnover rate $\gamma(x)$ of population x, with x between 0 and 1. The variable x represents the 'turnover class', with $x = 0$ the class with the highest turnover and $x = 1$ the class with the lowest turnover rate. The turnover rate function is

$$\gamma(x) = r\frac{x^h}{\theta^h + x^h}.$$

The three parameters are r the highest turnover rate (corresponding to class $x = 0$), θ the fraction of cells with turnover rates higher than $r/2$ and h a measure of heterogeneity (a large value of h means that there is a clear separation between a renewing and a nonrenewing fraction).

For scenario XPOP, the variable x acts as a population structure variable, like the age a does. Therefore, formally we need to introduce a new PDE, along with an initial condition and a boundary condition to describe the scenario. Because cells always stay in the same turnover class, the new PDE associated to scenario XPOP is similar to the original PDE.

$$\text{(PDE XPOP)} \qquad \underbrace{\frac{\partial n(t,a,x)}{\partial t}}_{\text{change in person age}} + \underbrace{\frac{\partial n(t,a,x)}{\partial a}}_{\text{change in cell age}} = \underbrace{-\gamma(x)n(t,a,x)}_{\text{loss of cells in turnover class } x},$$

$$\text{(Initial Condition XPOP)} \qquad n(t=0,a,x) = \underbrace{\begin{cases}\delta(a) & \text{if } x\in[0,1],\\ 0 & \text{otherwise,}\end{cases}}_{\text{all cells aged 0 initially}}$$

$$\text{(Boundary Condition XPOP)} \qquad n(t,a=0,x) = \underbrace{r(x)}_{\text{cell birth}}.$$

Here, the initial cell density is uniform over the interval [0,1], i.e., each turnover class contains the same density of cells. Because all cells are replaced and cells cannot move from one class to another, the cell density will stay uniform over [0,1] at any age of the person. The parameter h controls which proportion of the cells have a high-turnover rate, by setting a threshold on x over which the turnover rate function $\gamma(x)$ falls off rapidly. In practice, to solve numerically the PDE for scenario XPOP, it is necessary to discretize the variable t, a and x, so x can be considered as a discrete class. We have used 17 turnover classes linearly spaced between 0 and 1: $x = i/16$, $i = 0,\ldots, 16$. This way, scenario XPOP can be simulated by the numerical methods developed for the other scenarios.

2POPE (3 Parameters: r, θ, f). This is a combination of Scenario 2POP with Scenario E. The three parameters are the fraction of renewing cells, the initial death rate and the half-death constant.

Death rate of the renewing subset: $\gamma(t,a) = \gamma(a) = r\theta/(\theta + a)$.

Birth rate of the renewing subset is given by the Volterra equation introduced in Scenario E.

Fraction of renewing subset: f constant.

Fitting the Model to the Data

Computing the ^{14}C Concentration Associated to a Scenario

Solutions for the cell density $n(t,a)$ can be computed numerically by integrating directly the PDE, given the initial condition and boundary condition. The boundary and initial condition solution is (Bernard et al., 2010)

$$n(t,a) = [N_0\delta(t-a) + \beta(t-a)]exp\left(-\int_0^a \gamma(t-a+s,s)ds\right).$$

The first term accounts for the cells that were formed during development, and the second term accounts for the cells that were born after development. (A similar solution exists for scenario XPOP). The average ^{14}C level $\tilde{C}$ of a DNA sample of a person born at calendar year D_{birth}, and having started development at $D_{dev} = D_{birth} - t_0$, and collected at calendar year D_{coll} (here this is the date of death of the person), is

$$\tilde{C} = \frac{\int_0^{t_{death} = D_{coll} - D_{dev}} \overbrace{K_{lag}(D_{coll} - a)n(t,a)}^{\text{contribution of cells aged } a \text{ to } ^{14}C} \, da}{\underbrace{N(t)}_{\text{total number of cells}}}.$$

The function K_{lag} is a food-lag atmospheric ^{14}C level curve. When evaluated at calendar year y, $K_{lag}(y)$ represents the actual ^{14}C concentration that will integrate newly synthesized DNA, and will therefore correspond to an average of past atmospheric concentration, to account for the food supply chain, from photosynthesis to the table. The initial cell number N_0 does not enter explicitly in the equation for $\tilde{C}$, since it appears as a factor on the numerator and the denominator.

We had previously used a discrete shift function: $K_{lag}(y) = K(y - t_{lag})$ (Spalding et al., 2013). This means that the atmospheric carbon would take at time t_{lag} to reach dividing cells.

Although more complex food-lag functions could be more realistic, such as a Gamma kernel, here we used the discrete shift, with $t_{lag} = 1$ year, consistent with previous parameter exploration for hippocampal cells (Spalding et al., 2013). ^{14}C content measured from blood serum in Swedish residents revealed a lag of 1.5 ± 0.7 years (Georgiadou et al., 2013), very close to the lag we used.

Nonlinear Regression

To estimate the goodness-of-fit of a parameter set, we looked at a weighted sum of square of the errors (SSE) between the calculated (predicted) ^{14}C concentrations $(\tilde{C})$ and the measured ^{14}C concentration (C). The SSE is

$$SSE = \sum_{i=1}^{n} \left(\tilde{C}_i - C_i\right)^2 w_i^2.$$

The weights represent the confidence assigned to each sample i, so that a sample with a large confidence w_i will penalise the SSE more than a sample with a small confidence, for equal squared difference $(\tilde{C}_i - C_i)^2$. The weights are normalized so that

$$\sum_{i=1}^{n} w_i^2 = 1.$$

As a measure of confidence of sample i, we used the amount of carbon measured, to define a value c_i

$$c_i = \begin{cases} m & m<20\mu g, \\ 20 & m \geq 20\mu g. \end{cases}$$

The weight w_i is

$$w_i = \frac{c_i}{\left(\sum_{i=1}^{n} c_i^2\right)^2}.$$

To compare how good each scenario fits the data, we used the least-square version of the Akaike Information Criterion corrected for small sample sizes (Burnham and Anderson, 2002),

$$AIC_c = n \log \frac{SSE}{n} + 2K + \frac{2K(K+1)}{n - K - 1},$$

where n is the number of samples, and K the total number of parameters in the model (including SSE/n), i.e., $K = p + 1$, where p is the number of parameters of the scenario. A small value of AICc indicates that the scenario is close to the data. When comparing different scenarios, only differences between AICc values are relevant, so we report for each scenario the difference between its AICc and the best AICc and $\Delta AIC_c = AIC_c - min_i\, AIC_c$.

Global Parameter Estimates

We have estimated the best parameter sets for each subset and scenario by minimizing the SSE. We then compared the values of the AICc to find out the most appropriate scenario for each cell subset. Table S6 shows the main parameter estimation results.

Individual Turnover Rates Estimates

For scenario A, the birth-and-death model has a single parameter, which can in principle be estimated for each sample. It is therefore possible to obtain a turnover rate estimate from a single sample. For the other scenarios, more than one parameter need to be estimated, which cannot be done for each sample individually, unless some parameters are fixed. Scenario 2POP fitted well for most of the subsets, indicating that cell populations were heterogeneous in terms of renewal dynamics. Using the renewing fractions

that best fitted each subset, the turnover rate within the renewing fraction could be estimated for individual samples. Renewing fractions used for each subset were: NeuN+ 0.25; SOX10+ 0.73; NeuN-/SOX10− 0.85; DARPP32+ 0.16; DARPP32−/NeuN+ 0.23; NeuN− 0.48; NeuN+ HD 0.035; SOX10+ HD 1.0; NeuN-/SOX10− 0.47; Unsorted 0.50.

In some cases, it was not possible to fit the measured ^{14}C level using these renewal fractions, either because the renewing fraction would be larger, or because the exact fit would predict a negative turnover rate. However, for the comparison of turnover rates, is was important to keep the renewing fractions equal for all samples, so samples that could not be fitted were considered as outliers.

Numerical Methods

All simulations were performed with MATLAB (version R2012b). Solutions for the PDEs and the carbon concentration model were integrated numerically. The atmospheric ^{14}C level curve was sampled at midpoint each year (1993.5, 1994.5, …) and linearly interpolated to convert it to a continuous function for use in the numerical integral functions.

We used the nonlinear optimization function fminsearch to find parameter sets that minimize the SSE. Different initial parameter guesses were used to ensure that the best fits were global minima. Then we used a Markov chain Monte Carlo method to explore the space in a systematic way. This allowed us not only to confirm that the parameter sets that minimized the SSE were most probably the best fits (that is, with a SSE globally minimal), but also, in certain case, to estimate the uncertainty on the parameter values. With the Monte Carlo method, we sampled the parameter space for scenario 2POP, and for the best scenario based on the ΔAICc. For each simulation, 50,000 points were sampled and the first 5,000 were discarded (the burnin).

Statistical Analysis

The median was used as a measure of centrality of the individual turnover rates, due to the presence of outliers. Mann-Whitney test was used for testing difference of median between different groups. Individual turnover rates based on scenario A were used when the groups did not have the same renewing fractions and turnover rates based on scenario 2POPA were used when the groups had the same renewing fractions. Scenarios were ranked according to the AICc.

SUPPLEMENTAL REFERENCES

Bernard, S., Frisén, J., and Spalding, K.L. (2010). A mathematical model for the interpretation of nuclear bomb test derived 14C incorporation in biological systems. Nucl. Instrum. Methods Phys. Res. B *268*, 1295–1298.

Burnham, K.P., and Anderson, D.R. (2002). Model selection and multi-model inference: a practical information-theoretic approach, Vol, Second Edition (New York: Springer Verlag).

Georgiadou, E., Stenström, K.E., Uvo, C.B., Nilsson, P., Skog, G., and Mattsson, S. (2013). Bomb-pulse 14C analysis combined with 13C and 15N measurements in blood serum from residents of Malmö, Sweden. Radiat. Environ. Biophys. *52*, 175–187.

Perthame, B. (2007). Transport equations in biology. Frontiers in Mathematics (Basel: Birkhäuser Verlag).

Tuttle, A.H., Rankin, M.M., Teta, M., Sartori, D.J., Stein, G.M., Kim, G.J., Virgilio, C., Granger, A., Zhou, D., Long, S.H., et al. (2010). Immunofluorescent detection of two thymidine analogues (CldU and IdU) in primary tissue. J. Vis. Exp. *Dec. 7*, pii: 2166.

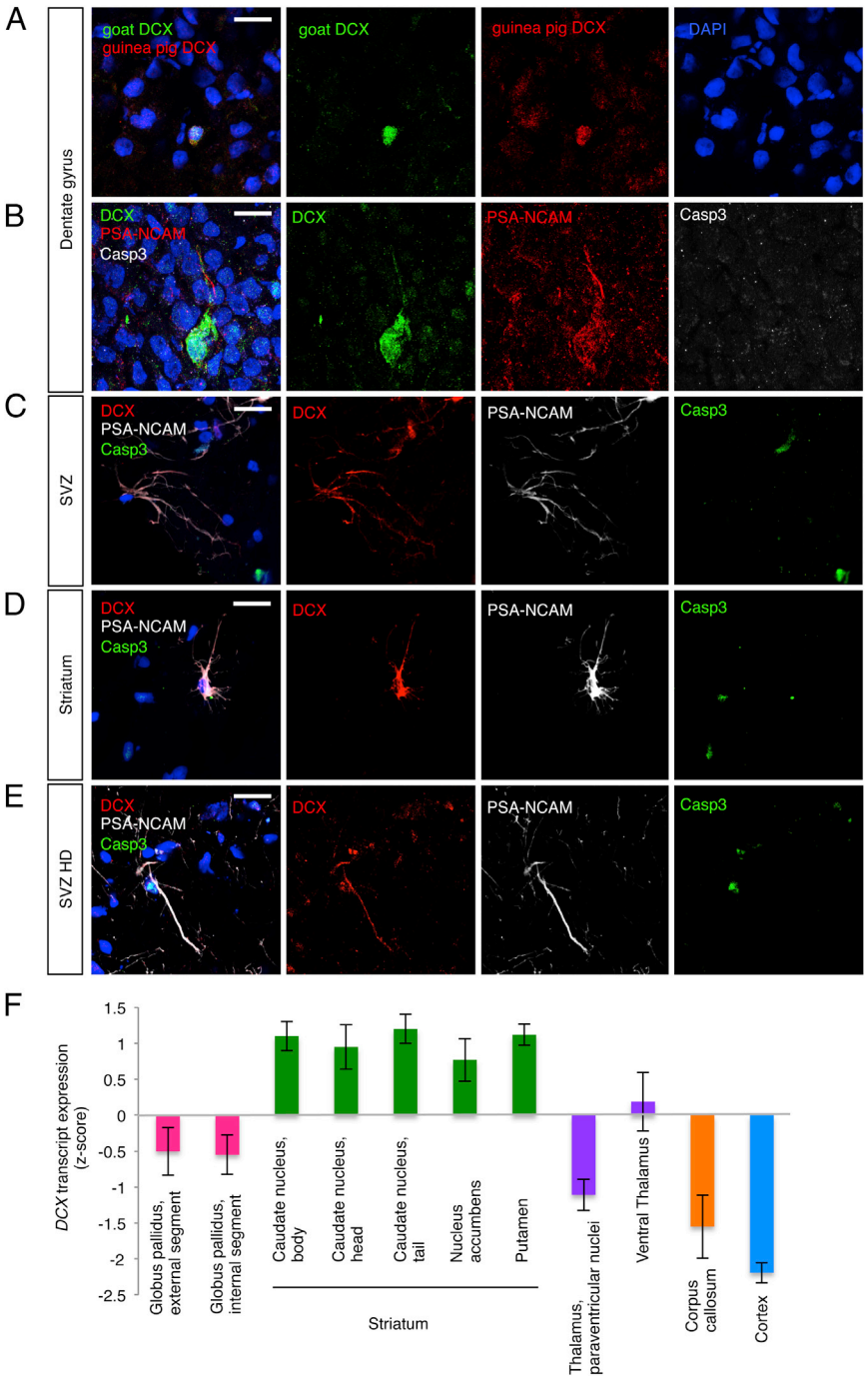

Figure S1. Neuroblast Marker Expression in the Dentate Gyrus of the Hippocampus, in the Subventricular Zone and in the Striatum, Related to Figure 1

(A–E) Two different DCX antisera label the same cells (A). The guinea-pig-derived antiserum was used in the western blot in Figure 1B. The majority of DCX-positive cells coexpress the neuroblast marker PSA-NCAM and all of them are negative for the apoptotic marker cleaved caspase 3 (B–D). Apoptotic DCX-positive cells are seen in the subventricular zone (SVZ) of patients affected by Huntington's disease (HD) (E). Scale bars, 20 μm.

(F) Comparison of z-score-normalized *DCX* mRNA expression in the human striatum, other regions close to the lateral ventricle and in the nonneurogenic cortex. The subjects are aged 21 to 57, n = 6 (data from the Allen brain atlas). Error bars show standard deviation between subjects.

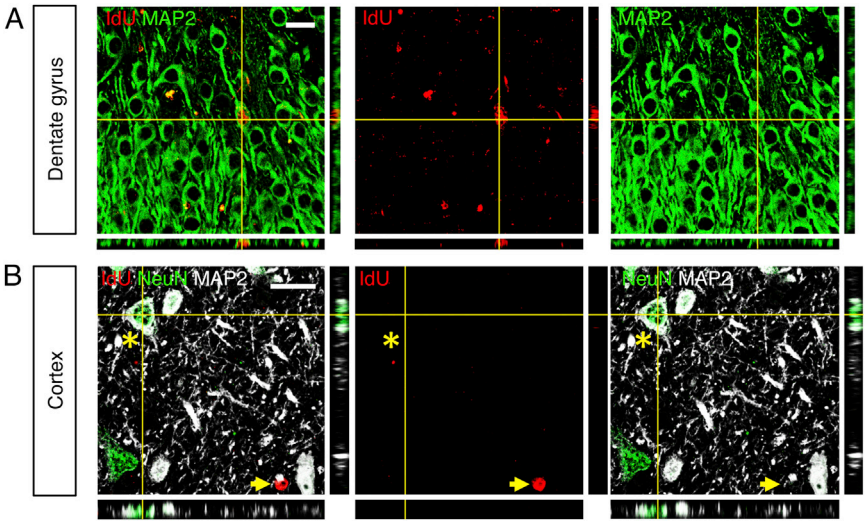

Figure S2. IdU Incorporation in Neurogenic and Nonneurogenic Regions, Related to Figure 2

(A) Newly generated neurons can be detected in the adult human dentate gyrus of the hippocampus in patients previously receiving IdU. Confocal images with orthogonal projections show an IdU-labeled neuron expressing MAP2.

(B) In nonneurogenic regions like the cortex, IdU-labeled nonneuronal nuclei are detected (arrow) but neurons are not IdU-labeled (star). Scale bars, 20 μm.

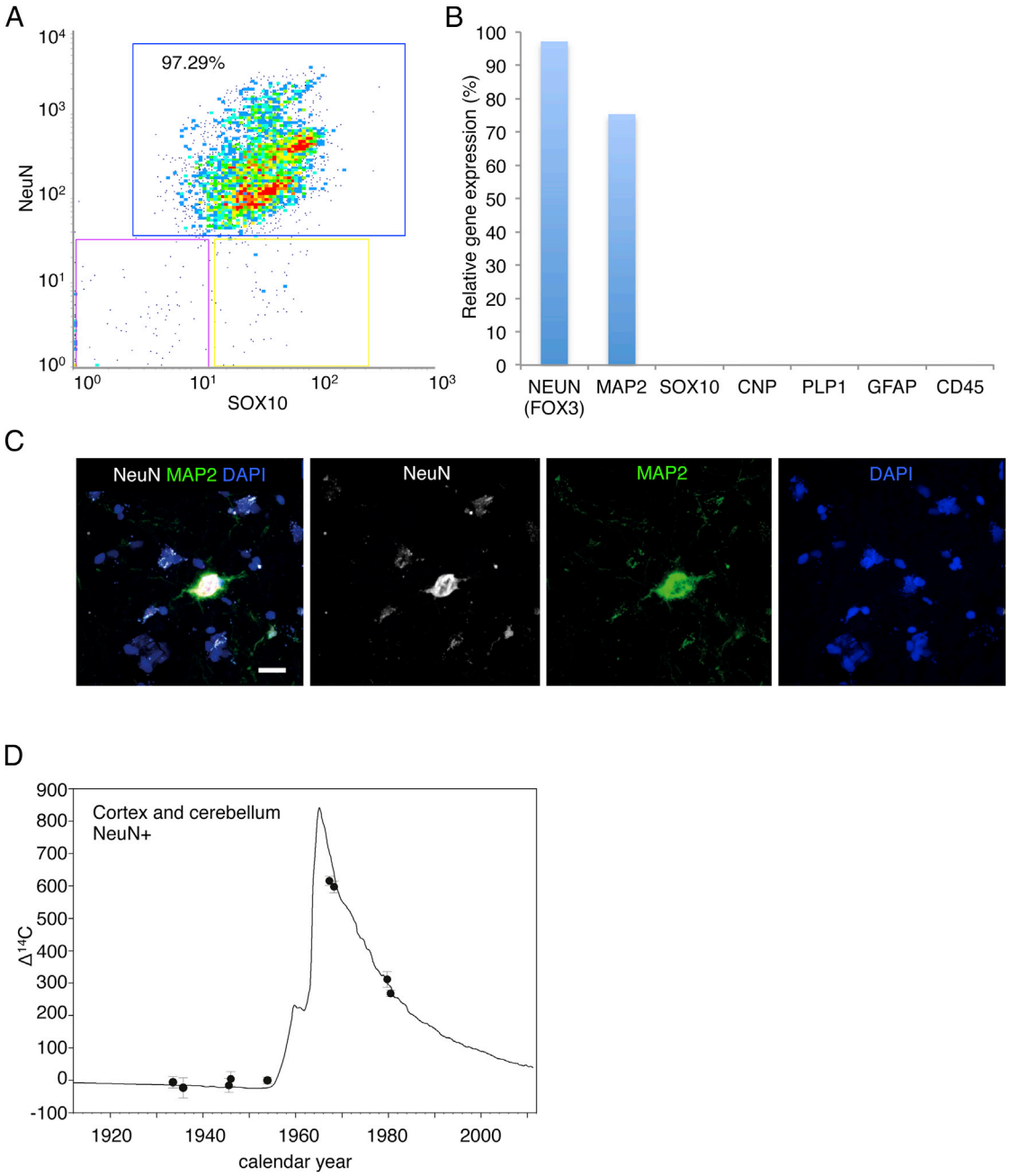

Figure S3. Validation of the Strategy for Retrospective Birth-Dating of Neuronal Nuclei, Related to Figure 4

(A) Reanalysis of flow-cytometry-sorted neuronal nuclei.

(B) Gene expression analysis of flow cytometry-isolated nuclei shows high expression of neuronal markers NeuN and MAP2 in the NeuN-positive fraction. In contrast, marker genes for oligodendrocyte lineage cells (SOX10, CNP, PLP1) and marker genes for astrocytes (GFAP) and hematopoietic cells and microglia (CD45) are not expressed in NeuN+ sorted nuclei (C). The antibody to NeuN labels neurons in the lateral wall of the lateral ventricle and in the striatum, as confirmed by the expression of the neuronal marker MAP2. Scale bar, 20 μm. Error bars indicate two standard deviations in ^{14}C concentration in the respective DNA sample.

(D) ^{14}C concentrations in genomic DNA from neuronal nuclei isolated from the cerebellum and from the occipital cortex do not significantly differ from atmospheric ^{14}C concentrations at birth.

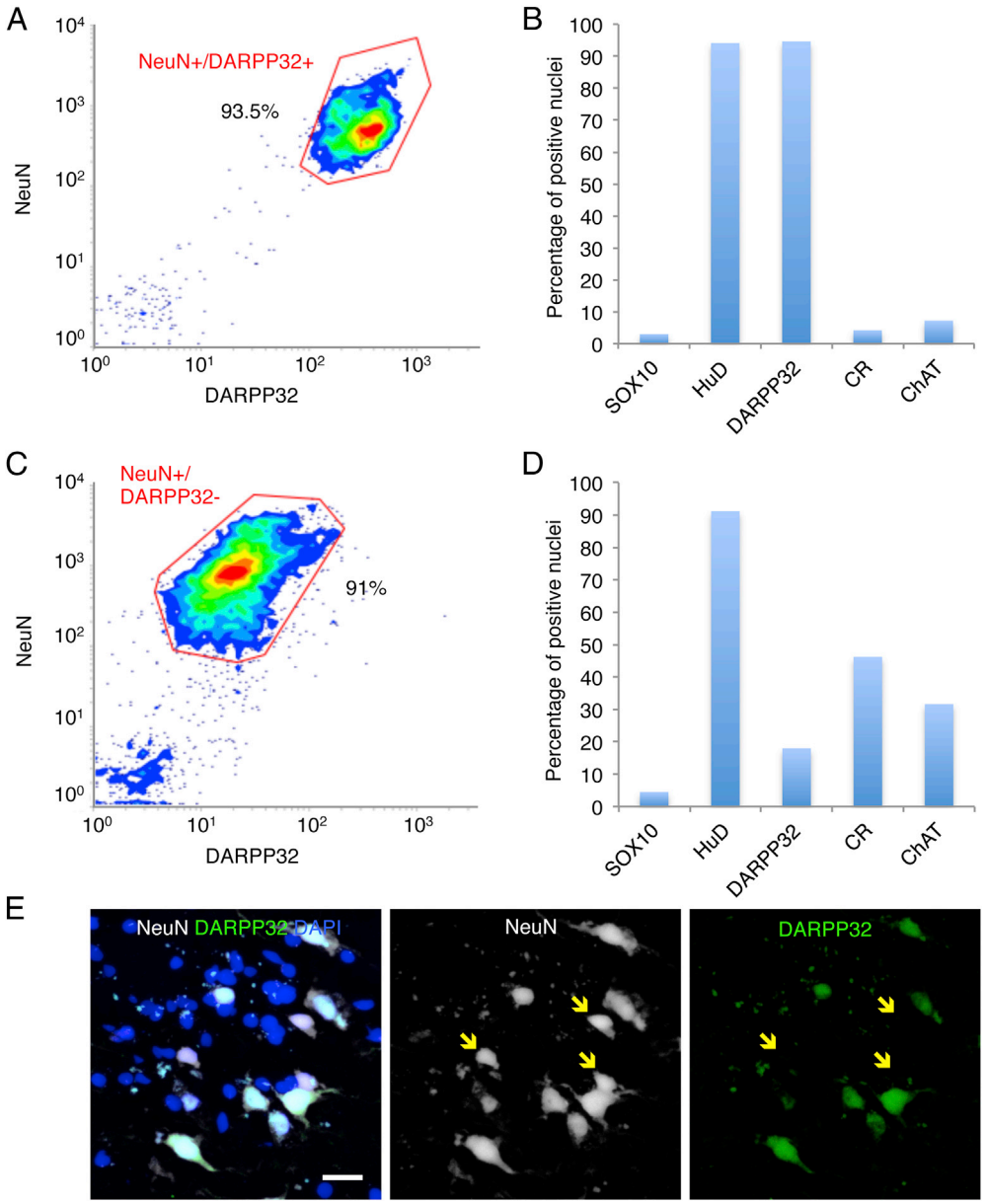

Figure S4. Validation of the Strategy for Retrospective Birth-Dating of Medium Spiny Neurons and Interneurons, Related to Figure 5

(A) Reanalysis of flow-cytometry-sorted medium spiny neuron nuclei (NeuN+/DARPP32+).

(B) Immunofluorescence analysis of flow cytometry-isolated NeuN+/DARPP32+ nuclei shows a high percentage of nuclei positive for the neuronal marker HuD and for the medium spiny neuron marker DARPP32. In contrast, oligodendrocyte lineage marker SOX10 and interneuron markers calretinin (CR) and choline acetyltransferase (ChAT) are expressed only in a small percentage of nuclei and/or attached cytoplasm.

(C) Reanalysis of flow-cytometry-sorted interneuron nuclei (NeuN+/DARPP32−).

(D) Immunofluorescence analysis of flow cytometry-isolated NeuN+/DARPP32− nuclei shows a high percentage of nuclei and/or attached cytoplasm positive for the neuronal marker HuD and for the interneuron markers calretinin (CR) and choline acetyltransferase (ChAT). In contrast, oligodendrocyte lineage marker SOX10 and medium spiny neuron marker DARPP32 are expressed in a small fraction of nuclei only.

(E) Antibodies to NeuN label all neurons in the striatum, whereas DARPP32 expression is specific to medium spiny neurons, which constitute the vast majority of the striatal neurons. The minority population of striatal interneurons is defined by the presence of NeuN and the absence of DARPP32 (arrows). Scale bar, 20 μm.

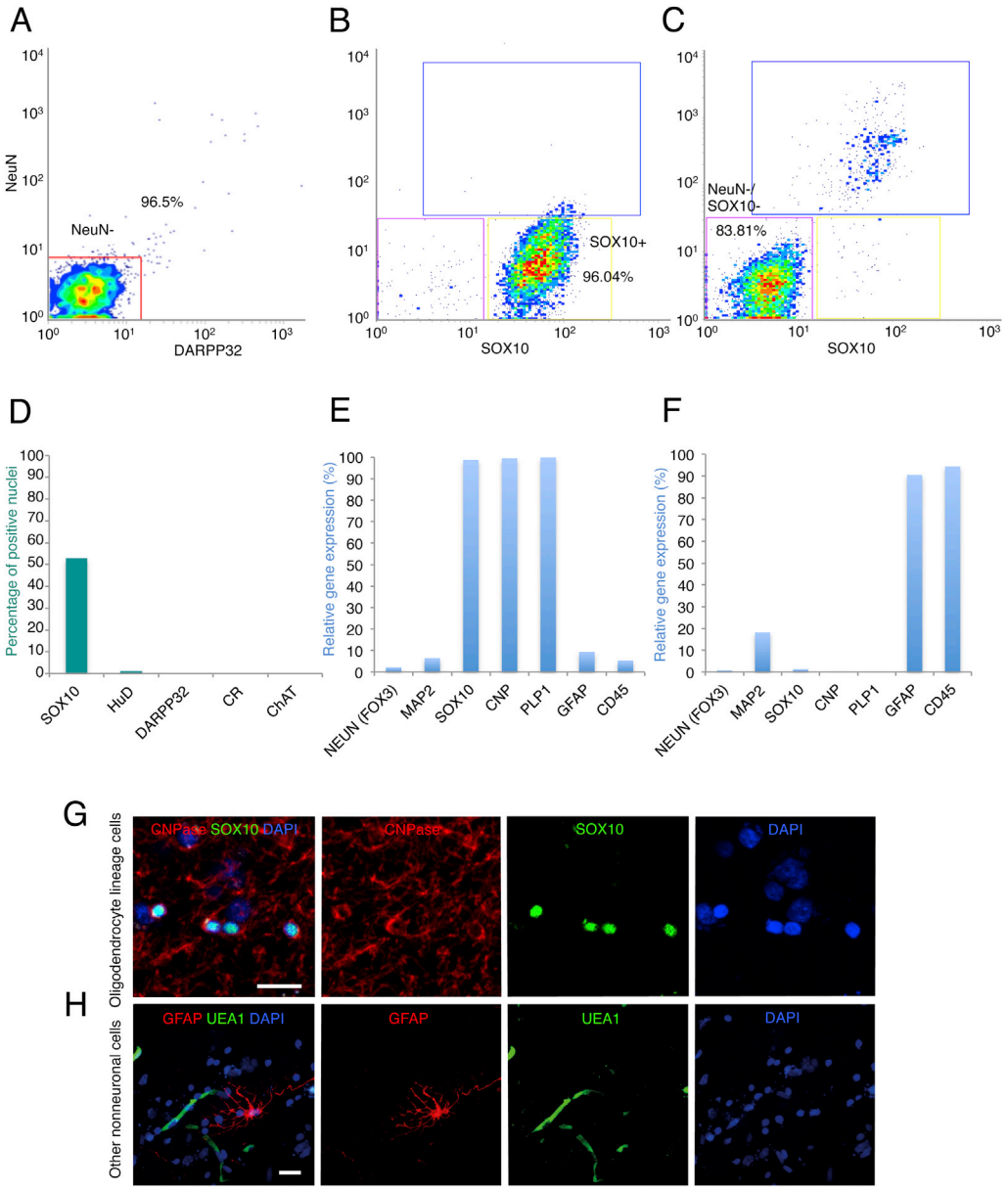

Figure S5. Validation of the Strategy for Retrospective Birth-Dating of Nonneuronal Cell Nuclei, Related to Figure 6

(A–C) Reanalysis of flow cytometry sorted nonneuronal cell nuclei (NeuN-, A), oligodendrocyte lineage cell nuclei (SOX10+, B) and nonneuronal and nonoligodendrocyte lineage nuclei (NeuN-/SOX10−, C).

(D) Immunofluorescence analysis of flow cytometry isolated NeuN-nuclei shows a high percentage of nuclei positive for the oligodendrocyte lineage marker SOX10, whereas neuronal marker HuD, medium spiny neuron marker DARPP32 and interneuron markers calretinin (CR) and ChAT are only expressed in a very small fraction of nuclei and/or attached cytoplasm.

(E and F) Gene expression analysis of flow cytometry-isolated nuclei shows high expression of marker genes for oligodendrocyte lineage cells (SOX10, CNP, PLP1) in the SOX10+ fraction (E). In contrast, marker genes for astrocytes (GFAP) and hematopoietic cells and microglia (CD45) are highly expressed in the NeuN-/SOX10− sorted nuclei (F).

(G) SOX10 labels oligodendrocyte lineage cells, as confirmed by the expression of CNPase.

(H) NeuN-/SOX10− cells comprise astrocytes identified by GFAP expression, endothelial cells identified by UEA1 expression and other cell types.

Scale bars, 20 μm.